Coastal flooding from wave overtopping and sea level rise adaptation in the northeastern USA

Coastal Engineering 150 (2019) 39–58

Contents lists available at ScienceDirect

Coastal Engineering

journal homepage: www.elsevier.com/locate/coastaleng

Coastal flooding from wave overtopping and sea level rise adaptation in the northeastern USA

Dongmei Xie[a,b], Qing-Ping Zou[c,*], Anthony Mignone[d], Jean D. MacRae[b]

[a] College of Harbour, Coastal and Offshore Engineering, Hohai University, Nanjing, 210098, China
[b] Department of Civil and Environmental Engineering, University of Maine, Orono, ME, 04469, United States
[c] The Lyell Centre for Earth and Marine Science and Technology, Institute for Infrastructure and Environment, Heriot-Watt University, Edinburgh, UK
[d] National Weather Service, Caribou, ME, 04736, United States

ARTICLE INFO

Keywords:
Coastal flooding
Wave-current interaction
Wave overtopping
Seawall
Coastal adaptation
Coastal resilience
Sea level rise
Climate change
ADCIRC
SWAN
Urban flooding

ABSTRACT

In the northeastern United States, flooding arising from wave overtopping poses a constant threat to coastal communities during storm events. The purpose of this study is to construct a novel integrated atmosphere-ocean-coast and overtopping-drainage modeling framework based on the coupled tide, surge and wave model, SWAN + ADCIRC, to assess risk and facilitate coastal adaptation and resilience to flooding in a changing climate in this region. The integrated modeling system was validated against the field observations of water level, wave height and period during the January 2015 North American blizzard. The water level collected by a sensor in the Avenues Basin behind the seawall in Scituate, Massachusetts were combined with the basin relationship between basin area and water level given by the USGS LIDAR data to obtain the field measurements of wave overtopping water volume in order to verify the model predictions. At the storm peak, the significant wave height was increased by 0.7 m at the coast by tide and surge. The wave setup along the coast varied from 0.1 m to 0.25 m depending on the coastline geometry. The interaction between tide-surge and waves increased the wave overtopping rate by five folds mainly due to the increased wave height at the toe of the seawall. The wave overtopping discharge would approximately double in an intermediate sea level rise scenario of 0.36 m by 2050 for a storm like the January 2015 North American blizzard. The wave overtopping discharge would increase by 1.5 times if the seawall crest elevation was raised by the same amount as sea level rise as an adaptation strategy. An increase of 0.9 m in the seawall crest elevation instead of 0.6 m currently planned by the town is required to bring the wave overtopping discharge to the current level under a 0.36 m sea level rise scenario. This result is primarily due to larger waves arriving at the seawall without breaking in the presence of larger water depth.

1. Introduction

Low-lying coastal communities are vulnerable to flooding due to elevated water level, large battering waves or the combined effect of both during storm events (Kirshen et al., 2008; National Research Council, 2009; NOAA, 2018). Coastal flooding may occur due to functional and structural failures of natural barriers or coastal defenses under three scenarios: (1) the water level exceeds the crest elevation of natural barriers or coastal defenses, (2) waves rush up the shore and overtop the crest of natural barriers or coastal defenses, and (3) natural barriers or coastal defenses are breached or undermined (Sallenger, 2000; Zou et al., 2013). According to the US Billion-dollar Weather/Climate Disaster report by the National Oceanic and Atmospheric Administration's National Centers for Environmental Information, the aggregated loss due to storm surge and wave damage in US coastal areas reached approximately 700 billion dollars for major storm events between 1980 and 2017 (NOAA, 2018). The risk of coastal flooding and vulnerability of our critical infrastructure will increase with sea level rise and intensification of storminess due to climate change (Nicholls, 2002; Kirshen et al., 2008; Emanuel, 2013; Woodruff et al., 2013; Lin et al., 2016; Douglas et al., 2017; Roberts et al., 2017). The global mean sea level is predicted to rise on the order of 0.3–1.0 m by 2100 under the presumed low to high greenhouse gas emission scenarios (Church et al., 2013). Nicholls (2002) identified enhanced storm flooding and lowland inundation as one of the four major impacts of sea level rise. Kirshen et al. (2008) concluded that the current 100-year storm surge elevation in the northeastern United States may be exceeded every 70 years–30 years by 2050 under low to high greenhouse gas emission scenarios respectively. At more exposed locations like Boston, Massachusetts (MA), the recurrence interval of the current 100-year storm

* Corresponding author.
E-mail address: q.zou@hw.ac.uk (Q.-P. Zou).

https://doi.org/10.1016/j.coastaleng.2019.02.001
Received 17 October 2017; Received in revised form 5 December 2018; Accepted 5 February 2019
Available online 07 February 2019

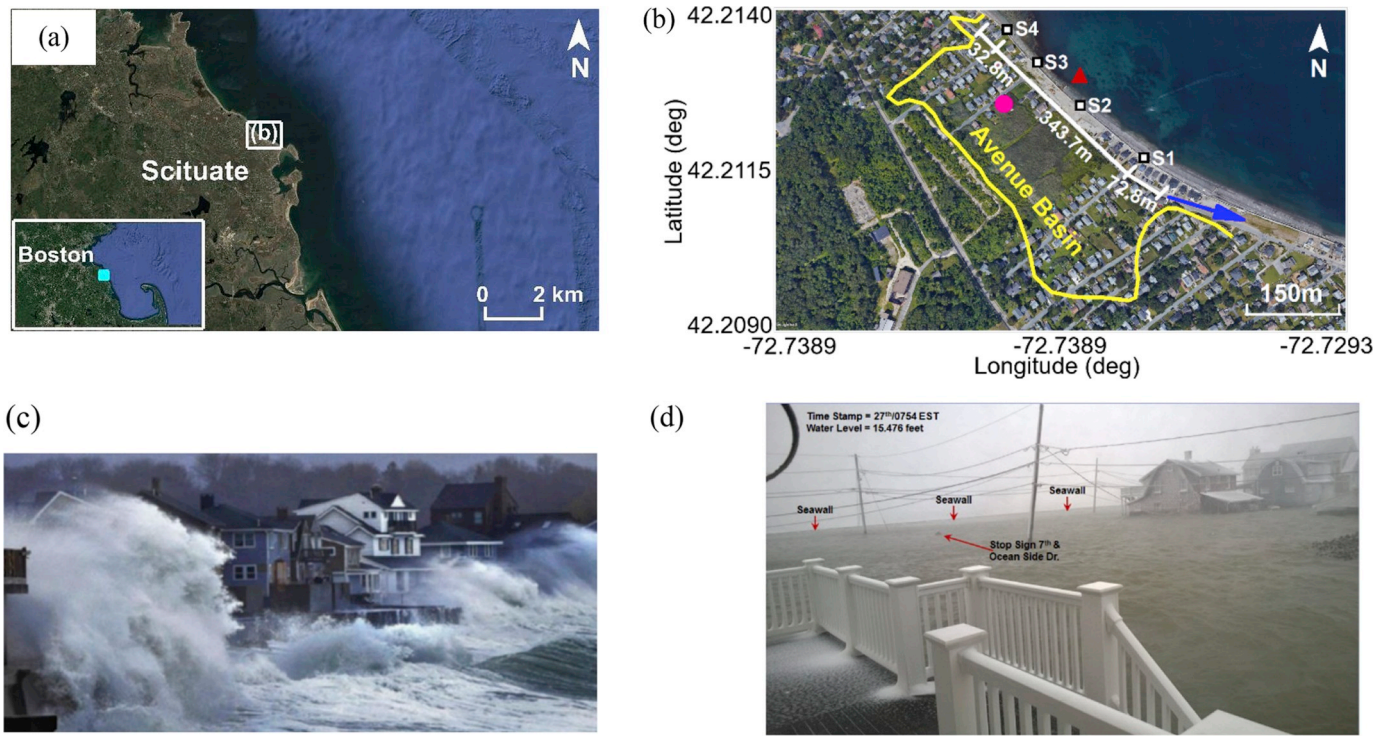

Fig. 1. (a) The location of Scituate, Massachusetts (small cyan square in the subplot at the lower left corner) and its seawall (small white square in the center) relative to Boston. (b) The zoom-in view of Avenues Basin indicated by the small white square in Fig. 1a. The yellow solid line outlines the basin area at the elevation of 5.0 m above local mean sea level, which is approximately the measured water level by a data logger at the peak of the storm. It indicates the inundated area at the peak of the storm. The white line marks the 449.3 m seawall. The pink circle marks the Solinst LTC Levelogger Edge in the Avenues Basin. The red triangle shows the drainage pipe on the seaside of the basin. The blue arrow represents the corridor through which the water flows out of the Avenues Basin. The four white squares S1 to S4 mark the locations of the cross-shore beach profile survey seaward from the seawall. (c) The wave overtopping at the Scituate seawall on March 03, 2013 (http://www.gazettenet.com/home/4968871-95/storm-thursday-snow-areas). (d) The Avenues Basin flooded by wave overtopping water at the seawall on January 15, 2015. (For interpretation of the references to colour in this figure legend, the reader is referred to the Web version of this article.)

surge elevation may be even reduced to 8–30 years by 2050 (Kirshen et al., 2008).

Along the northeastern coast of the United States, various coastal defenses, e.g. seawalls, revetments, groins and jetties, have been built to protect buildings and infrastructure from storms and to prevent damage due to flooding and erosion. In Massachusetts, 586 km of the 1770 km coastline is protected by coastal structures and 360 km, or 20 percent of the coastline, is protected by seawalls. Wave overtopping and seawall breaches caused major flooding during severe storms (See Fig. 1; MADCR, 2009; MACZM, 2013a). Massachusetts is expecting and planning for 0.12–0.55 m and 0.25–2.08 m sea level rise by the year of 2050 and 2100 respectively (MACZM, 2013b). The town of Scituate, MA, for example, has experienced its worst flooding in recent years and is planning to elevate the seawall by 0.60 m to prepare for future flooding and sea level rise (MACZM, 2016). It is critical to predict water level and waves during storms to assess the capacity of seawalls to protect communities from future storms and provide guidance for the design of coastal structures.

Coastal flooding prediction presents several challenges: (1) accurate description of processes at various spatial and temporal scales, (2) geometric complexities of the coastal environment (natural barriers, seawalls), (3) nonlinear hydro-morphological interactions, (4) lack of field observation for model validation and (5) the uncertainty propagating from the meteorological forcing to coastal flood risk prediction (Du et al., 2010; Zou et al., 2013; Gallien et al., 2014). Coastal inundation models have become popular tools to achieve this objective over the past decade (e.g. Bates et al., 2005; Bunya et al., 2010; Dietrich et al., 2010; Kennedy et al., 2012; Chen et al., 2013; Zou et al., 2013; Gallien et al., 2014; Orton et al., 2016; Gallien, 2016). However, most studies of coastal flooding in the Eastern US focus on tropical instead of extratropical storms (Chen et al., 2008; Emanuel, 2013; Lin et al., 2016; Zhang et al., 2017; Marsooli and Lin, 2018). Most coastal inundation studies do not consider wave overtopping at coastal defenses. Only recently, a few studies have focused on coastal flooding due to wave overtopping using numerical models (Lynett et al., 2010; Zou et al., 2013; Gallien et al., 2014; Gallien, 2016; Tsoukala et al., 2016; Lerma et al., 2018). Also, there is a lack of field data of wave overtopping at the seawalls to validate the model predictions.

The hydrodynamic response of coastal defense is sensitive to the water level, wave height and period at the structure. Numerous studies have described the significant interactions between waves, currents, tides and storm surges (e.g. Cavaleri et al., 2007; Wolf, 2009; Dodet et al., 2013; Chen et al., 2015; Xie et al., 2016; Zou and Xie, 2016; Marsooli and Lin, 2018; Sun et al., 2018). Various mechanism of wave-current interactions including depth-averaged and depth-dependent wave radiation stress have been proposed in the past (Longuet-Higgins and Stewart, 1962, 1964; Mellor, 2005; Smith, 2006; Zou et al., 2006; Ardhuin et al., 2008; Ji et al., 2017).

The integrated tide-surge, wave and flooding modeling framework, therefore, is required to accurately predict the flooding due to wave overtopping. Currently, the literature on integrated atmosphere-ocean-coast-overtopping modeling of flooding due to wave overtopping at coastal structures is limited (Zou et al., 2013; Gallien et al., 2014; Gallien, 2016; Tsoukala et al., 2016; Lerma et al., 2018). Zou et al. (2013) used an ensemble integrated meteorological, tide and surge, nearshore and RANS-VOF surf zone hydrodynamic model to study coastal flood risk due to wave overtopping and quantify the uncertainty at each stage of the model cascade. Gallien et al. (2014) and Gallien (2016) integrated an overland flow model based on the shallow-water equations with wave overtopping and drainage models to produce

reliable urban flood predictions by resolving flood defenses and flow routing in transient conditions. Tsoukala et al. (2016) and Lerma et al. (2018) also used a downscaling modeling framework coupled with wave overtopping to study coastal flooding in a changing climate. This type of coastal flooding modeling requires resolution of processes with different spatial and temporal scales from ocean basin to coast to surf zone and the structures, e.g., wave-current and wave-tide-surge interactions and wave breaking.

Surf zone models for natural beaches range from the energy flux balance models (Goda, 1975; Thornton and Guza, 1983; Battjes and Stive, 1985), Boussinesq-type wave models (Wei et al., 1995; Kennedy et al., 2000; Chen et al., 2000; Shi et al., 2012), and nonlinear shallow water models (Brocchini and Dodd, 2008; Zijlema and Stelling, 2008; Smit et al., 2013) to sophisticated Reynolds-Averaged Navier-Stokes (RANS) solvers (Lin and Liu, 1998; Wang et al., 2009; Higuera et al., 2013).

Wave overtopping models range from empirical models based on extensive physical model tests (Hedges and Reis, 1998; Van der Meer et al., 2016), nonlinear shallow water equations (Hu et al., 2000), Boussinesq-type models (Lynett et al., 2010; McCabe et al., 2013) to RANS-VOF models (Lara et al., 2006; Losada et al., 2008; Reeve et al., 2008; Lv et al., 2009; Peng and Zou, 2011; Zou and Peng, 2011; Raby et al., 2019) and smoothed particle hydrodynamics (SPH) method (Shao et al., 2006). The empirical models have been widely used and provide a robust alternative to predict wave overtopping for the design of coastal structures (Van der Meer et al., 2016).

In the present study, we will develop an integrated atmosphere-ocean-coast-overtopping-drainage modeling framework following Zou et al. (2013). Xie et al. (2016) and Zou and Xie (2016) validated the application of the coupled wave and circulation model SWAN + ADCIRC in the Gulf of Maine during extratropical storms like the January 2015 North American blizzard. The SWAN + ADCIRC model will be coupled with a surf zone model, a wave overtopping model and a drainage model to predict flooding caused by wave overtopping at seawalls in this study. The water level data collected in the Avenues Basin in Scituate, Massachusetts during the January 2015 North American blizzard is combined with the relationship between basin area and elevation given by the USGS LIDAR data to obatain the field measurements of water volume changes in the basin due to overtopping to verify the model predictions.

The main objective of this work is to develop an integrated atmosphere-ocean-coast-overtopping model to accurately predict coastal flooding due to wave overtopping and sea level rise. Section 2 describes the site and field measurements. Section 3 focuses on the modeling approach. Model setup and parameters are defined and explained in Section 4. Section 5 discusses the results from the coupled wave and circulation model. Wave overtopping results are analyzed and discussed in Section 6. Conclusions are drawn in the final section.

2. Site description and field measurements

2.1. Site description

The town of Scituate, Massachusetts, with its 94.5 km coastline, is located approximately 40 km to the southeast of Boston (Fig. 1a). During winter storms, the coast is frequently subjected to large ocean waves generated by northeasterly winds in the Gulf of Maine. As a defense against wave attack, an extensive network of hard structures has been constructed, including concrete seawalls, stone masonry seawalls, revetments, and stone jetties which extend for approximately 32 km. A basin located along Oceanside Drive behind the seawall in the northern part of Scituate (Fig. 1a), locally known as the Avenues Basin, is periodically flooded due to storm waves overtopping the seawall and overwhelming the drainage system. For example, during the January 2015 North American blizzard, the water level was below the seawall crest elevation along the Scituate coast throughout the storm. The flooding of the basin was caused by wave overtopping the seawall instead of overflow. The basin drainage system consists of a 0.9 m outlet pipe that runs from the Oceanside Drive, under the seawall to discharge to the ocean (Fig. 1b). The outlet pipe is fitted with a flap gate to prevent ocean water from entering the drainage system during elevated tide levels. Although the Avenues Basin is a closed basin area, once the water level reaches an elevation of 4.36 m above local mean sea level, water begins to flow out of the basin through a corridor parallel to Ocean Drive at the southeast corner as indicated by the blue arrow in Fig. 1b. Incoming water can overwhelm the drainage flow rate and water level continues to rise until the top of the seawall is reached at an elevation of 5 m above local mean sea level. The length of the seawall contributing to flooded water by wave overtopping is 449.3 m in total. The northern part of the seawall is 32.8 m and the wave overtopping rate along this section is represented by the wave overtopping rate at S4. The middle part of the seawall is 343.7 m and wave overtopping rate along this section is the average value at S2 and S3. The southern part of the seawall is 72.8 m and the wave overtopping rate along this section is represented by the wave overtopping rate at S1.

The Avenues Basin has been flooded due to wave overtopping during several major storms, e.g., the Northeastern United States blizzard of 1978 (February 7, 1978), the 1991 Perfect Storm (October 31, 1991), the December 2010 North American blizzard (December 27, 2010), the Early February 2013 North American blizzard (February 9–10, 2013), the January 2015 North American blizzard (January 27, 2015) and the January 2016 United States blizzard (January 27, 2016).

2.2. January 2015 North American blizzard

The January 2015 North American blizzard was a powerful and destructive extratropical storm that swept along the coast of the northeastern United States in the late January of 2015. The lowest recorded pressure was 970 hPa and the highest wind gust reached 42.5 m/s. From January 27 to 28, the storm moved northeastward off the Mid-Atlantic coast to the east coast of Canada as depicted in Fig. 2a. The track of the storm maintained a northeasterly wind wave fetch across the Gulf of Maine in the cold air mass for the entire event. When the air temperature stays below the ocean surface temperature, the ocean surface boundary layer becomes much more unstable thus transporting higher winds to the ocean surface. Another important meteorological feature of the storm was the presence of a strong elongated high-pressure system to the north of the region (Fig. 2b). The interaction of the two pressure systems strengthened the pressure gradient across the Gulf of Maine, and the east-west elongation of the high-pressure system produced a long fetch distance. The presence of the high-pressure system also impeded the forward movement of the low-pressure system, which resulted in a long duration of winds across the fetch area. The strong northeasterly wind in the fetch area generated a pronounced storm surge and large waves. The storm tide corresponded to a 6-year return period event in Boston, Massachusetts. The significant wave height measured by the wave buoy east of Boston reached 8.29 m. Significant flooding was reported in Scituate and seawalls were damaged at some other coastal locations in Massachusetts during this storm (MACZM, 2016). Time evolution of water level in the Avenues Basin in Scituate due to wave overtopping was measured by a sensor during this storm.

2.3. Field measurements

A Solinst LTC Levelogger Edge, which combines a datalogger, a Hastelloy pressure sensor, a temperature detector and a conductivity sensor, was deployed to measure the water level, temperature and conductivity in the Avenues Basin during storms. Contained in a PVC pipe, the device was secured to a telephone pole at an elevation of 2.78 m above local mean sea level next to a staff gauge on 7th Avenue in the basin prior to several storm events. The datalogger was set to

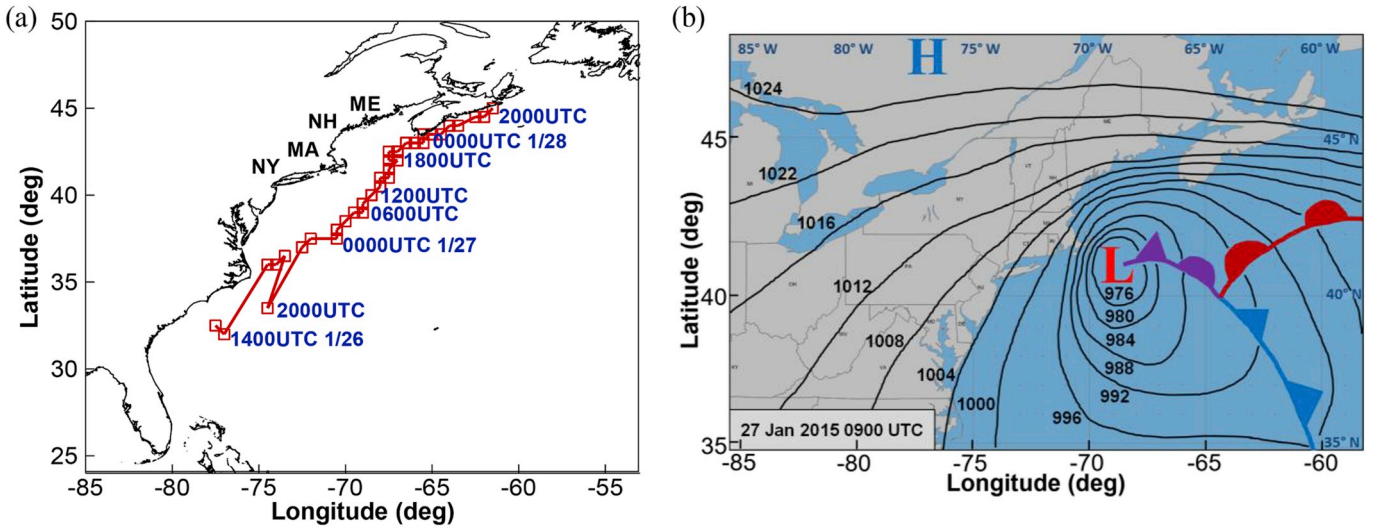

Fig. 2. The January 2015 North American blizzard. (a) The storm track: the red solid line with squares marks the track; NY, MA, NH and ME denotes the state of New York, Massachusetts, New Hampshire, and Maine; (b) Surface atmospheric pressure analysis at 9:00 UTC, 1/27/2015. Intense low pressure to the southeast of Scituate in conjunction with strong high pressure to the north produces a strong northeasterly wind fetch across the Gulf of Maine. "L" denotes low pressure and "H" denotes high pressure. The solid blue line with triangles marks the cold front. The solid red line with semicircles marks the warm front. The solid purple line with semicircles and triangles marks the occluded front. The isobars are drawn for every 4 hPa. (For interpretation of the references to colour in this figure legend, the reader is referred to the Web version of this article.)

record water level at a 6-min interval, which was chosen to be the same as the time interval of the data collection at the nearest tide gauge in Boston Harbor. Since the LTC Levelogger Edge measures the absolute pressure, which include both the water pressure and the atmospheric pressure, a Solinst Barologger Edge was used to compensate for the atmospheric pressure fluctuations to obtain water level. The volume of water in the basin was estimated by combining the measured water depth from the bottom of the Avenues Basin with the basin area determined by the USGS LIDAR data (Heidemann, 2014). The water level gradients due to wind set-up and seepage could potentially affect the estimation of water volume in the basin. However, these two processes were relatively small compared to the outflow and overtopping water volume considered here. The field measurements were used to validate the model prediction of wave overtopping at the seawall.

The water level recorded by the datalogger during the January 2015 North American blizzard is shown in Fig. 3b. The data logger began to collect data when the water level in the basin reached 2.78 m above local mean sea level. The area of the basin was determined by plotting the USGS LIDAR data of topography in the basin at 0.3048 m elevation contour intervals using ArcGIS. The area in square meters was then calculated for each 0.3048 m slice from the bottom of the basin at an elevation level of 2.48 m to the seawall crest at 5.00 m above the local mean sea level. To translate the water level recorded by the data logger to the volume of water in the basin, a 4th order polynomial curve was fit to the basin area data derived using ArcGIS (Fig. 3a) and the water volume in the basin was obtained by integrating the area data over the whole range of water level (Fig. 3b). During the January 2015 North American blizzard, the maximum water level in the basin reached the crest of the seawall at 10:24 UTC on January 27. The corresponding peak accumulated water volume in the basin was 166,509 m^3 (Fig. 3b).

The basin is 449.3 m long along the seawall and approximately 100.0 m long across the seawall, which is small in dimension (Fig. 1b). When an equilibrium state is reached, the water level gradient in the basin due to local wind can be estimated by the following formula (Pugh, 1987):

$$\frac{\partial \zeta}{\partial x} = \frac{C_D \rho_A W^2}{g \rho D} \tag{1}$$

Where $\frac{\partial \zeta}{\partial x}$ is the horizontal water level gradient, C_D is the surface drag coefficient, ρ_A is the air density, W is wind speed, g is gravitational acceleration, ρ is water density, D is local water depth. The estimated water level gradient in the basin is 0.000024 by assuming $W = 15\ m/s$, $D = 2.0\ m$ at the storm peak. Since the wind was blowing from northeast across the seawall during the storm, it can be obtained that the water level difference at the two ends of the basin across the seawall is 0.0024 m, which is negligible.

About 449.3 m of seawall along the Avenues Basin contributes to the flooding through overtopping. As shown in Table 1, the crest elevation of the seawall is 5.0 m above local mean sea level along its entire length. Site surveys were conducted at four locations S1−S4 (Fig. 1b) along the seawall to obtain the toe elevations of the seawall. The cross-shore profiles from the seawall to the end of the foreshore at these four locations were then determined by combining the site survey data with USGS LIDAR data. Fig. 4 shows the sketch of the cross-shore profile at site S2 (Fig. 1b). The beach profiles consist of two sections: a steep slope adjacent to the seawall and a mild slope further offshore. The steep slope is treated as a sloping structure in this study and the mild slope further offshore is treated as the foreshore in front of the structure. Table 1 lists the site survey data necessary for overtopping prediction, including the crest elevation of the vertical wall, the toe elevation of the vertical wall, the steep slope in front of the vertical wall, the toe elevation of the steep slope and the mild slope further offshore.

3. Methodology

In this study, an integrated multiscale modeling framework was developed to investigate the impacts of tide, surge and waves on coastal flooding in the northeastern United States (Fig. 5). The integrated modeling system consists of four components: (i) a tide, surge and wave coupled hydrodynamic model SWAN + ADCIRC (Dietrich et al. (2011, 2012) spanning from the oceanic to nearshore region; (ii) a surf zone model by Goda (1975, 2009); (iii) a wave overtopping model (Van der Meer et al., 2016) and (iv) a drainage model (Henderson, 1966) to estimate the discharge from the basin behind the seawall. The surface wind and pressure outputs from the NCEP Climate Forecast System Version 2 (CFSv2) (Saha et al., 2014) and the tidal forcing from the global model of ocean tides TPXO (Egbert et al., 1994) were used to drive the coupled tide, surge and wave model, SWAN + ADCIRC, to obtain the seaward boundary conditions for the surf zone model. SWAN

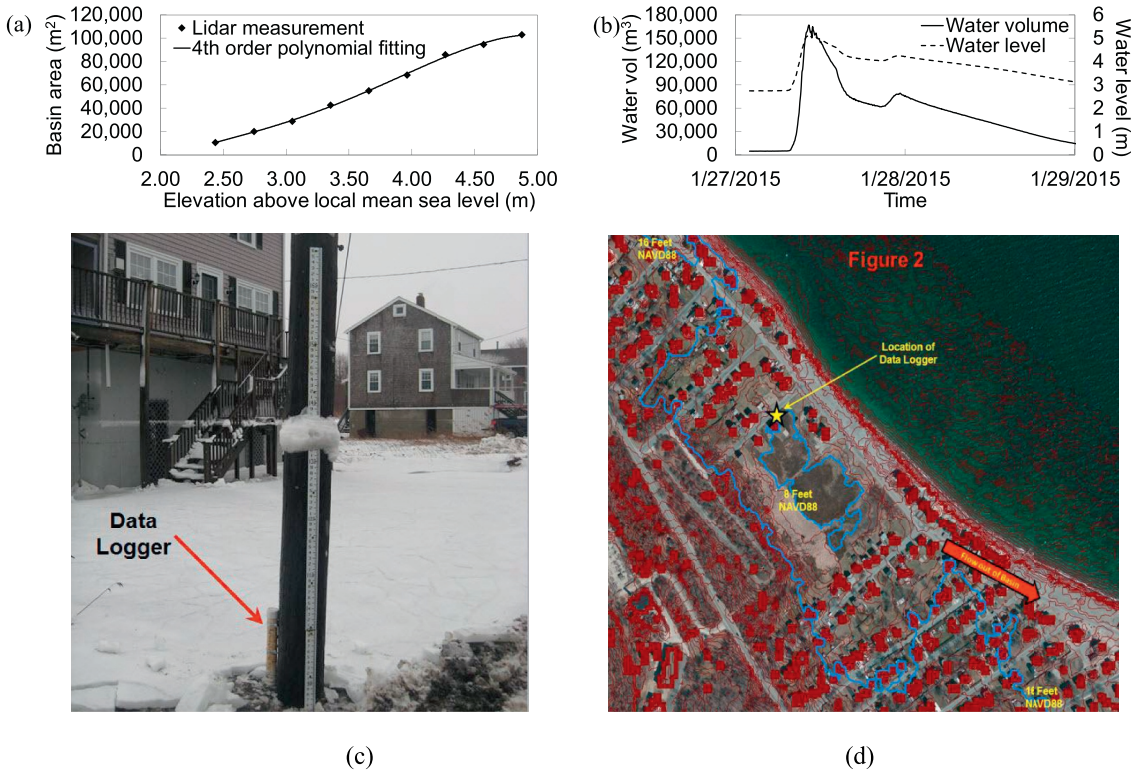

Fig. 3. (a) The relationship between the basin area and elevation above the local mean sea level according to the USGS Lidar data and its 4th order polynomial fit; (b) Water level recorded by the datalogger (dashed line) is combined with the relationship between basin area and water level from (a) to obtain the corresponding water volume in the Avenues Basin (solid line) during the January 2015 North American blizzard. (c) Blue lines are the topographic contour lines and border lines of the inundated area for water level above the local mean sea level at 16 feet/5.03 m and 8 feet/2.59 m measured by the data logger in the Avenues Basin during the January 2015 North American blizzard. The red lines are additional topographic contours in 1 foot intervals. Yellow star indicates the location of the data logger for water level measurements (d) Photo of the data logger in front of a house. (For interpretation of the references to colour in this figure legend, the reader is referred to the web version of this article.)

is a phase-averaged wave model, which cannot properly account for wave reflection from the seawall or capture wave breaking and turbulence properly at the bathymetry and grid resolution adopted in this study. Along the Scituate coast, the 3-arcsecond digital elevation model of the Gulf of Maine was used and its resolution is approximately 90 m. Even if we increase the grid resolution of the unstructured grid considerably at the expense of much more CPU time, the resolution of bathymetry along the Scituate coast is fixed, therefore, does not allow accurate predictions of wave parameters at the toe of the seawall. However, there is a steep beach in front of the seawall, so that the wave at the toe of the seawall is not saturated and is dependent on incident wave conditions. Therefore, the surf zone model by Goda (1975, 2009) was used to propagate waves from the seaward edge of the surf zone to the toe of coastal defenses in this study. The wave parameters and water level at the toe of the structures predicted by the surf zone model were then fed into a wave overtopping model to predict the coastal flooding due to overtopping. The water volume in the basin was then calculated by subtracting the water drained from the total water volume that overtops the seawall.

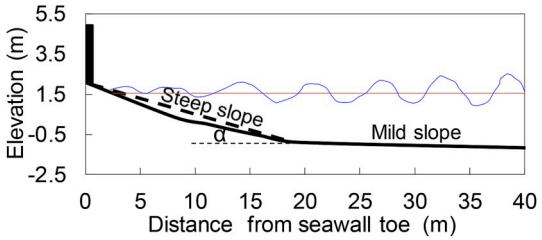

Fig. 4. The sketch of the cross-shore beach profile from the seawall to the end of foreshore at S2 location seaward from the seawall indicated in Fig. 1b.

3.1. Tide, surge and wave models

The interaction between surface gravity waves and tide-surge and wave-current interaction is important during severe storms both over continental shelf and at coastal waters (Brown and Wolf, 2009; Wang and Sheng, 2016; Wang et al., 2017; Sun et al., 2018). Wang and Sheng (2016) found current-induced modification of wind energy input to the

Table 1
Detailed information of the seawalls and beach profiles in front of the Avenues Basin in Scituate, MA, at the four locations S1, S2, S3 and S4 along the seawall indicated in Fig. 1b. All elevations here are referred to local mean sea level in Scituate, MA.

Site	Crest elevation of vertical wall (m)	Toe elevation of vertical wall (m)	Steep slope adjacent to seawall α (−)	Toe elevation of the steep slope (m)	Mild slope offshore (−)
S1	5.00	2.82	0.125	−0.87	0.021
S2	5.00	2.08	0.154	−0.87	0.021
S3	5.00	1.19	0.113	−0.87	0.036
S4	5.00	2.74	0.148	0.04	0.032

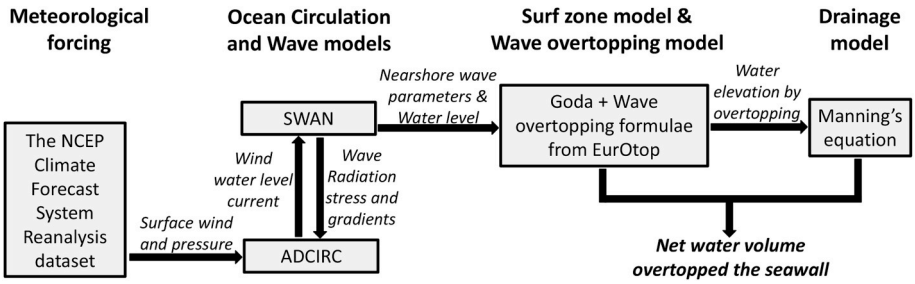

Fig. 5. Integrated modeling system for coastal flooding arising from wave overtopping at a seawall.

wave generation, and current-induced wave advection and refraction can change the significant wave height and peak wave period by 10 percent. Wave breaking may be induced by spatially varying opposing current (Chen and Zou, 2018; Zou and Chen, 2017). Waves may also be responsible for observed intense currents (Wang et al., 2017). It is thus important to use a coupled ocean circulation and spectral wave model to obtain the accurate prediction of wave parameters as well as ocean circulation in coastal waters.

The two-dimensional (2D) depth-integrated ADCIRC (ADCIRC-2DDI) was used to investigate the hydrodynamics associated with tide and surge in the northeastern coast of United States. Originally developed by Luettich and Westerink (2004), the ADCIRC-2DDI solves the depth-integrated shallow water equation on an unstructured triangular mesh using a coupled discontinuous-continuous Galerkin finite element method (Dawson et al., 2006). By adopting an unstructured triangular mesh, the ADCIRC-2DDI model provides considerable flexibility in resolving complex geometry and bathymetry while maintaining computational efficiency. ADCIRC utilizes the Generalized Wave Continuity Equation (GWCE) formulation. When integrating the GWCE by parts over the horizontal computational domain, the integral of the outward flux per unit width normal to the boundary is obtained, which allows tidal waves to propagate out of the domain. In this study, the Avenues Basin is mainly used to measure the total overtopping water volume, therefore, treated as a bathtub without carrying out a 2D ADCIRC simulation of the inundated basin. ADCIRC also includes a robust wetting and drying algorithm, which enables it to simulate inundation due to overflow over a structure. However, it cannot cope with wave overtopping.

The third-generation spectral wave model Simulating WAves Nearshore (SWAN) solves the wave action balance equation for wave spectra of random short-crested, wind-generated waves and swell based on winds, bottom topography, tides and currents (Booij et al., 1999; Ris et al., 1999). The model is particularly applicable in coastal waters because it accounts for several shallow water wave processes, i.e., triad-wave interaction, depth-induced wave breaking and bottom friction dissipation. Zijlema (2010) adapted the original SWAN code on structured grid to run on an unstructured grid by using a vertex-based, fully implicit, finite difference algorithm.

Dietrich et al. (2011, 2012) integrated SWAN and ADCIRC model where the wave-current-tide-surge interaction is included through the wave radiation stress, current refraction and water depth modulation of waves. The two-way coupled model allows seamless information exchange between the two model components by running on the same unstructured mesh. For practical implementation, ADCIRC first interpolates the wind field at 10 m above the ocean surface and atmospheric pressure at the ocean surface on each node of the shared unstructured mesh and solves the generalized wave continuity equation for water level and depth-integrated current. It then passes the wind stress, water level and current to SWAN. SWAN solves the wave action balance equation and integrates over the spectral domain for wave radiation stress, which is subsequently passed back to ADCIRC to be included in the vertically-integrated momentum equation for a new calculation of water level and current. The information exchange between the two model components happens at the same interval as the integration time step of SWAN.

3.2. Surf zone model

The calculation of wave overtopping at coastal structures requires wave height and period at the toe of the structures. Since the prediction of wave height and period by SWAN is no longer accurate in the surf zone, the surf zone model by Goda (1975, 2009) is used instead to propagate waves from the seaward edge of the surf zone to the toe of coastal defenses in this study. Goda (1975) proposed an empirical formula based on the compilation of laboratory results of wave breaking for random waves. In Goda's model, the breaker index, which is the ratio of limiting breaker height to water depth is dependent on the bottom slope and the relative water depth. The breaker index is expressed as follows,

$$\frac{H_b}{h_b} = \frac{A}{h_b/L_0}\left\{1 - \exp\left[\frac{\pi h_b}{L_0}(1 + 15\tan^{4/3}\theta)\right]\right\} \tag{2}$$

Where H_b and h_b are wave height and water depth when wave breaks. L_0 is deepwater wave length corresponding to the spectral mean wave period. $\tan\theta$ is the bottom slope given in Table 1. When applied for irregular waves, the empirical constant A is set at 0.18 for the upper limit and 0.12 for the lower limit of the triangular cut of the probability density function of the Rayleigh distribution (Papoulis and Pillai, 2002).

The actual formulae for approximation of significant wave height at the shoreline are as follows.

$$H_{1/3} = \begin{cases} K_s H_0' & : h/L_0 \geq 0.2 \\ min\{(\beta_0 H_0' + \beta_1 h),\ \beta_{max} H_0',\ K_s H_0'\} & : h/L_0 < 0.2 \end{cases} \tag{3}$$

Where K_s is the shoaling coefficient and is calculated based on linear wave shoaling theory (Dean and Dalrymple, 1984). H_0' is the equivalent deep water significant wave height with the inclusion of wave refraction. h is the still water depth. The three coefficients β_0, β_1 and β_{max} are calculated as below.

$$\left.\begin{aligned} \beta_0 &= 0.028(H_0'/L_0)^{-0.38} exp[20\tan^{1.5}\theta] \\ \beta_1 &= 0.52 exp[4.2\tan\theta] \\ \beta_{max} &= max\{0.92,\ 0.32(H_0'/L_0)^{-0.29}\exp[2.4\tan\theta]\} \end{aligned}\right\} \tag{4}$$

Goda's model (1975, 2009) is robust and considers the effect of several dynamic processes, e.g. wave setup and surf beats on breaking wave height. However, it is only applicable for unidirectional random waves propagating on a beach of uniform slope, and reasonable results are obtained for bottom slopes ranging from 1/200 to 1/10. The requirements of Goda's model were satisfied in this study.

3.3. Wave overtopping model

A phase-resolving wave model (e.g. FUNWAVE, SWASH) cannot predict overtopping at seawall but can be coupled with SWAN + ADCIRC model to predict the wave conditions and water level

at toe of the seawall. However, A phase-resolving wave model is computational demanding. The surf zone model by Goda (1975, 2009) in combination with empirical wave overtopping model provides an efficient alternative for inundation prediction. The EurOtop empirical model for wave overtopping (Van der Meer et al., 2016) was used in this study. The overtopping model for a vertical seawall used in Zou et al. (2013) is not adequate here because the foot of the vertical seawall in Scituate, MA is submerged and connected with a relatively steep beach slope. The vertical seawall and the steep slope are treated as part of an integral structure, with the seawall being a wave wall on top of a steep slope embankment (see Appendix A). The empirical formulae from EurOtop (Van der Meer et al., 2016), in which the wave overtopping discharge per unit width is scaled by the relative freeboard, i.e. the height difference between the structural crest and the instantaneous water level, were applied for the corresponding simplified structural configuration. Based on EurOtop (Van der Meer et al., 2016), the dimensionless wave overtopping discharge is calculated as follows:

(1) With submerged wave wall toe

$$\frac{q}{\sqrt{g*H_{m0}^3}} = \frac{0.023}{\sqrt{\tan\alpha}}\gamma_b*\xi_{m-1,0}*\exp\left[-\left(2.7*\frac{R_c}{\xi_{m-1,0}*H_{m0}*\gamma_b*\gamma_f*\gamma_\beta*\gamma_v}\right)^{1.3}\right] \quad (5)$$

with a maximum of

$$\frac{q}{\sqrt{g*H_{m0}^3}} = 0.09*\exp\left[-\left(1.5*\frac{R_c}{H_{m0}*\gamma_f*\gamma_\beta*\gamma^*}\right)^{1.3}\right] \quad (6)$$

(2) With emerged wave wall toe

$$\frac{q}{\sqrt{g*H_{m0}^3}} = 0.09*\exp\left[-\left(1.5*\frac{R_c}{H_{m0}*\gamma^*}\right)^{1.3}\right] \quad (7)$$

$$\gamma^* = \gamma_v = \exp\left(-0.56*\frac{h_{wall}}{R_c}\right) \quad (8)$$

Where q is the mean overtopping discharge. H_{m0} is the incident wave height at the toe of the structure. In this study, H_{m0} refers to the significant wave height at the toe of the steep slope in front of the seawall if not described otherwise. $\tan\alpha$ is the characteristic slope of the structure, $\xi_{m-1,0}$ is the breaker parameter, R_c is the crest freeboard, γ_b is the influence factor for a berm, γ_f is the influence factor for roughness elements on a slope, γ_β is the influence factor for oblique wave attack, γ_v is the influence factor for a wave wall, h_{wall} is the height of the wave wall.

When the toe of the wave wall is submerged, the wave wall is treated as a 1:1 slope while keeping the same relative freeboard. An iterative process is applied to determine the average slope of the integral structure since wave run-up is unknown. More details of the procedure for implementing the above overtopping model are given in Appendix A.

3.4. Drainage model

The water in the flooded Avenues Basin caused by wave overtopping flows out through a drainage pipe and the corridor of the Oceanside Drive at the southeast corner of the basin as described in Section 2.1. During storm events with large wave overtopping discharge, the water mainly flows out through the Oceanside Drive corridor after the water level in the basin reaches 4.36 m above local mean sea level and the flow rate through the drainage system is limited.

Manning's equation (Henderson, 1966) for open channel flow was used to estimate the flow rate through the Oceanside Drive. Manning's equation calculates steady uniform flow velocity in open channels as a function of Manning's roughness coefficient, hydraulic radius and friction slope.

$$V = \frac{1}{n}R^{2/3}S_f^{1/2} \quad (9)$$

Where V is flow velocity, n is Manning roughness coefficient, R is hydraulic radius of open channels, S_f is friction slope. For uniform flow, the friction slope S_f can be replaced by the bed slope of open channels S_0.

4. Model setup

4.1. Model domain and bathymetry

Accurate simulation of coastal circulation requires resolving processes ranging from channel-scale to ocean basins (Bunya et al., 2010; Warner et al., 2008; Zhang and Baptista, 2008). To develop a storm surge model at any location, three important factors are considered: (1) the accurate representation of bathymetric and geometric features by model grid, (2) appropriate boundary conditions and (3) the reasonable representation of resonant modes (Blain et al., 1994). While large domains are usually required to reasonably capture the physical responses and simplify the boundary conditions (Blain et al., 1994; Westerink et al., 1994), they can be computationally demanding. The unstructured mesh can accommodate larger domains for coastal ocean circulation and wave models with locally refined grids to resolve shallow bathymetry, steep bathymetric gradients and intricate shorelines (Hagen et al., 2001). Although we mainly focus on surge and wave response along the coast of the northeastern United States, the model grid is set up to cover the entire east coast to minimize the influence of open boundary conditions, while providing high resolution within regions of rapidly varying geometry and flow response (Blain et al., 1994; Westerink et al., 1994, 2008). The current model domain (Fig. 6) is an evolution of the Eastcoast domain by Blain et al., (1994) and Westerink et al. (1994) and the domain for the Gulf of Maine by Yang and Myers (2008), Xie et al. (2016) and Zou and Xie (2016). The model domain covers the western North Atlantic, the Caribbean Sea, the Gulf of Mexico and the Gulf of Maine. The open boundary of the domain is extended further to the east along the 56°W meridian compared to the Eastcoast domain to allow longer fetch for surge and wave generation. Also, because the open boundary is located primarily in deep-water, the impact of nonlinear processes is limited.

The bathymetric data in the model domain consists of 4 datasets: (1) the ETOPO1 1 arc-minute Global Relief Model by the National Geophysical Data Center (NGDC) of the National Oceanic and Atmospheric Administration (NOAA) (Amante and Eakins, 2009); (2) the 3 arc-second digital elevation model of the Gulf of Maine (Twomey and Signell, 2013); (3) the 1/3 arc-second digital elevation model of Portland, Maine (Lim et al., 2009); (4) the 1/9 arc-second USGS National Elevation Dataset (NED) for southern Maine (https://viewer.nationalmap.gov/viewer/). The NOAA VDatum software (http://vdatum.noaa.gov) was used to convert the dataset elevations to a mean sea level datum when applicable. The bathymetry, and locations of wave buoys and tide gauges are shown in Fig. 7. The wave buoys and tide gauges in Fig. 7b are listed in Tables 2 and 3, respectively.

The unstructured triangular mesh for the model domain consists of 245,838 nodes and 463,593 elements. The water surface elevation, flow velocity and wave spectra are computed at each node. The grid resolution ranges from 100 km in deep basin to 10 m at the coast, providing sufficient resolution for tide, surge and wave propagation at the coast without compromising computational efficiency. Along the Scituate coast, the grid resolution is 60–100 m.

4.2. Surface wind and pressure forcing

The coupled SWAN + ADCIRC requires a wind field at 10 m above the ocean surface and atmospheric pressure at the ocean surface as

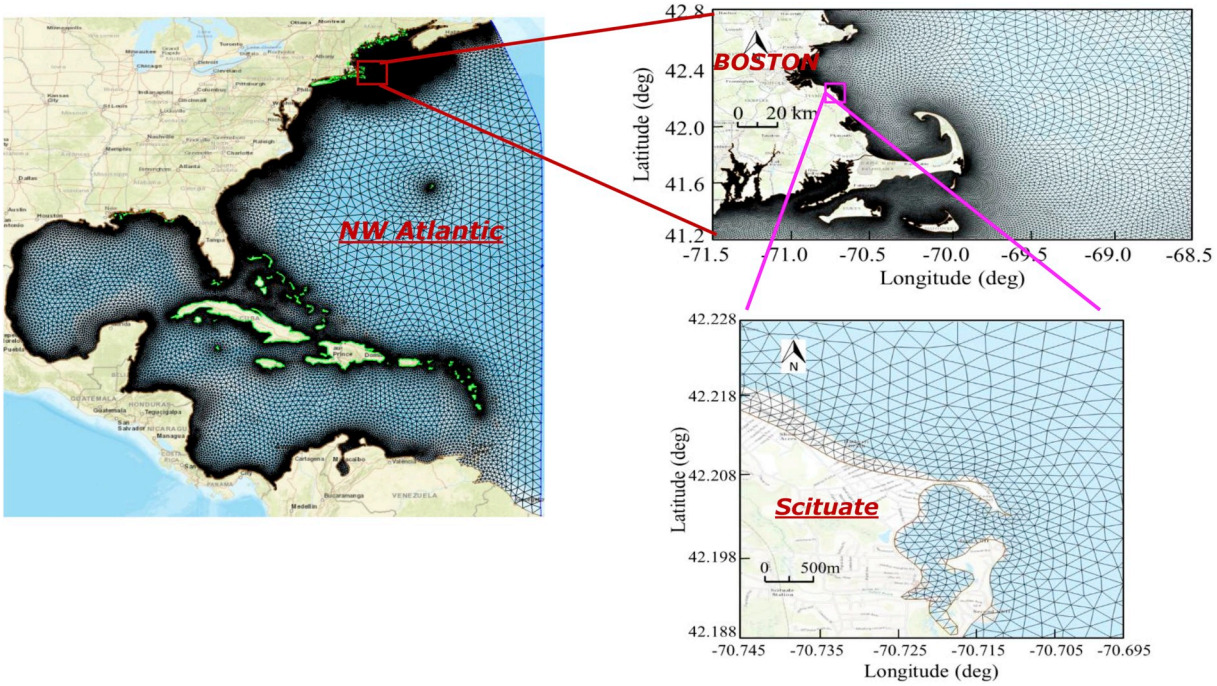

Fig. 6. Upper: Comparison of model domains for wave and surge modeling. The black solid line marks the model domain used in this study. The red solid line marks the Eastcoast model domain used by Blain et al., (1994) and Westerink et al. (1994). The blue solid line marks the model domain for the Gulf of Maine by Yang and Myers (2008), Xie et al. (2016) and Zou and Xie (2016). Lower: The unstructured grid system used in this study. (For interpretation of the references to colour in this figure legend, the reader is referred to the Web version of this article.)

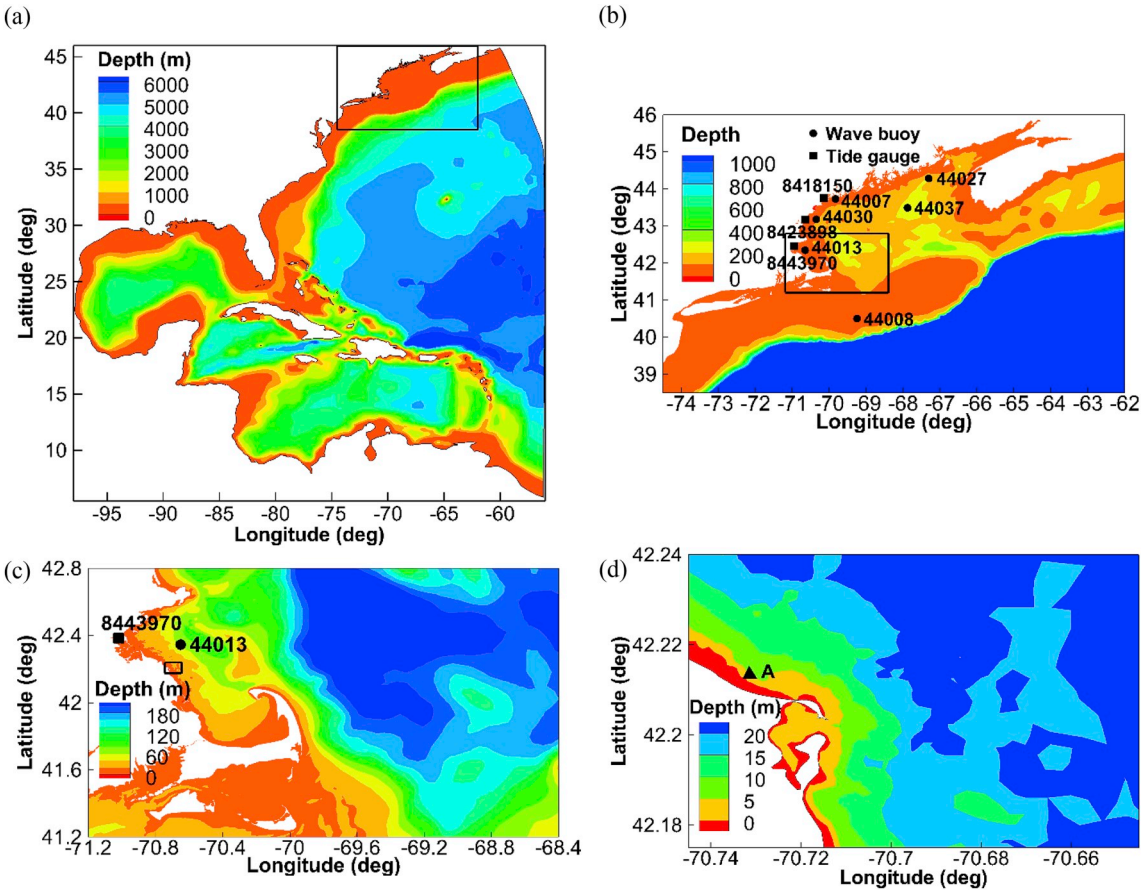

Fig. 7. The bathymetry within the model domain for (a) the east coast of United States. (b) Gulf of Maine indicated by the black rectangle in (a). The locations of wave buoys (circles) and tide gauges (squares). (c) Offshore of Massachusetts indicated by the black rectangle in (b). (d) The coast of Scituate, Massachusetts, indicated by the black rectangle in (c). The black triangle indicates the seawall.

Table 2
Wave buoys in the Gulf of Maine (see Fig. 7b for locations).

Wave buoy	Buoy location	Water depth/m
44008	Southeast of Nantucket, Massachusetts	66.4
44013	East of Boston, Massachusetts	64.5
44027	Southeast of Jonesport, Maine	178.6
44030	Western Maine Shelf	62.0
44037	Jordan Basin	285.0

Table 3
Tide gauges in the Gulf of Maine (see Fig. 7b for locations).

Tide gauge	Location	Water depth/m
8418150	Portland, Maine	11.5
8423898	Fort Point, New Hampshire	3.0
8443970	Boston, Massachusetts	5.0

inputs. Surface wind and pressure outputs from the NCEP Climate Forecast System Version 2 (CFSv2) (Saha et al., 2014) were used to drive the integrated modeling system in Fig. 5 to predict the storm surge, wave and wave overtopping at Scituate seawall during the January 2015 North American blizzard. The CFSv2 is a quasi-global, fully coupled atmosphere-ocean-land surface-ice model, which incorporates two data assimilation systems and two forecast models. The two assimilation systems provide the atmospheric, land surface and ocean initial conditions for model simulation. The CFSv2 model has a global coverage with 0.5-degree grid resolution and generates atmospheric output at hourly intervals.

4.3. Boundary conditions

The choice of boundary conditions can have a significant impact on the modeling results for the area of interest. To accurately predict those conditions, the tide and the storm-induced surge and waves at the open boundaries must be properly included. Since the open boundary for the coupled ADCIRC + SWAN model domain is placed mostly in deep ocean, the effects of shallow water nonlinear processes on the tide are ignored. The storm surge response is mainly an inverted barometric pressure effect at deep water and can be easily calculated. A decrease of 100 Pa in barometric pressure corresponds to a rise in sea level by 0.01 m. In this case, the storm surge due to the inverted barometric pressure effect was negligible. The storm tracked close to the east coast where the storm surge was significant, therefore the lateral boundary condition of storm surge near the Scotian Shelf was neglected. The waves generated outside of the model domain can propagate into the coupled ADCIRC + SWAN domain to account for the swell impact.

At the open boundary, both tidal response and waves were prescribed for the January 2015 North American blizzard. The eight most significant astronomical tide constituents (M2, S2, N2, K2, K1, P1, O1, Q1) were used. The harmonic constants were interpolated from the global model of ocean tides TPXO (Egbert et al., 1994). A SWAN model covering the North Atlantic was set up to run on a structured grid to generate 2D spectra at the boundary nodes that were subsequently used as the wave boundary condition for the coupled ADCIRC + SWAN model.

4.4. Model parameters

The two-dimensional depth-integrated version of ADCIRC was used to simulate the water level and circulation during the January 2015 North American blizzard. The wind stress was calculated by a standard quadratic law. The air-sea drag coefficient defined by Garratt's drag formula (Garratt, 1977) was used with a cap of $C_d \leq 0.0035$. Garratt's drag coefficient is widely used for storm surge modeling (e.g., Westerink et al., 2008; Bunya et al., 2010; Dietrich et al., 2010). The bottom stress was computed by the standard quadratic parameterization. The bottom friction coefficient was calculated using a Manning's n formation.

$$C_f = \frac{gn^2}{\sqrt[3]{H}} \tag{10}$$

Where C_f is the bottom friction coefficient, n is the Manning coefficient, H is the total water depth, g is gravitational acceleration. The Manning n was assigned at each node of the unstructured triangular mesh based on the USGS National Land Cover (Bunya et al., 2010). In the open ocean, the Manning n was assigned a value of 0.025.

The finite amplitude and convection terms were activated to include the nonlinear processes. A wetting and drying algorithm was applied as well. The lateral viscosity was set at 5 m^2/s for the ocean following Yang and Myers (2008) and 50 m^2/s for the land. The time step for ADCIRC was set to 0.5s to maintain computational stability.

The SWAN and ADCIRC models share the same unstructured mesh and surface wind forcing. The SWAN model was run with prescribed spectrum frequencies between 0.031384 and 1.420416 Hz, which was found to yield the best result when compared with buoy data during the sensitivity test by Zou and Xie (2016). The range was discretized into 40 bins on a logarithmic scale. The wave spectrum was solved in 360° with a directional resolution of 10°. The JONSWAP formulation (Hasselmann et al., 1973) was used for bottom friction. The friction coefficient of 0.038 m^2s^{-3} was used for both wind waves and swell (Zijlema, 2010). The time step for integration was set to 360 s.

The coupling interval at which information is passed between the models was the same as the time step for SWAN. ADCIRC passes wind stress, water level and currents to SWAN every 360 s, while SWAN passes radiation stress to ADCIRC to update the calculation of water level and current. A hyperbolic tangent function was applied for five days until the tidal component reached equilibrium prior to applying surface wind and pressure within the ADCIRC model.

Three cases were run: (1) tide-surge simulation without wave effects; (2) wave simulation without tide-surge and the associated current; (3) a fully coupled SWAN + ADCIRC run to include tide-surge and wave interactions.

5. Tide-surge and wave validation

The model-predicted tides were compared with the astronomical tide level obtained through harmonic analysis of gauge measurements at three tide gauges in the Gulf of Maine. Tide gauge 8443970 is the nearest to the area of interest and located approximately 31 km northwest of Scituate, MA. The tidal amplitudes and phases for the five major tidal constituents (M2, S2, N2, K1 and O1) in the Gulf of Maine were obtained using the MATLAB harmonic analysis toolbox T_Tide (Pawlowicz et al., 2002). The time period for harmonic analysis spans from 1:00 UTC 12/16/2014 to 0:00 UTC 2/1/2015. For simplicity, 1:00 UTC 12/16/2014 was used as the phase reference. Comparisons of observed and predicted tidal amplitudes and phases for the five major tidal constituents were carried out. The tidal amplitudes and phases were very well reproduced. The error of tidal amplitudes was in the range of 0.00–0.09 m. The dominant constituent M2 had an error of 0.07–0.09 m, accounting for 5–7 percent of the mean tidal amplitude. The error of tidal phases was less than 11°. The dominant constituent M2 had an error of 8°, accounting for 8 percent of the mean tidal phase.

A comparison of the predicted and observed water level at the three tide gauges is shown in Fig. 8. The model results with and without wave effect compared well with the tide gauge data. Increased storm surge level was observed at the three tide gauges when the wave effects were included. In shallow water, breaking waves generate radiation stress, which forces water onshore. The resulting cross-shore wave radiation stress gradient is balanced in turn by an increased pressure gradient. At the storm peak, the wave setup was 0.14 m at both tide gauge 8423898

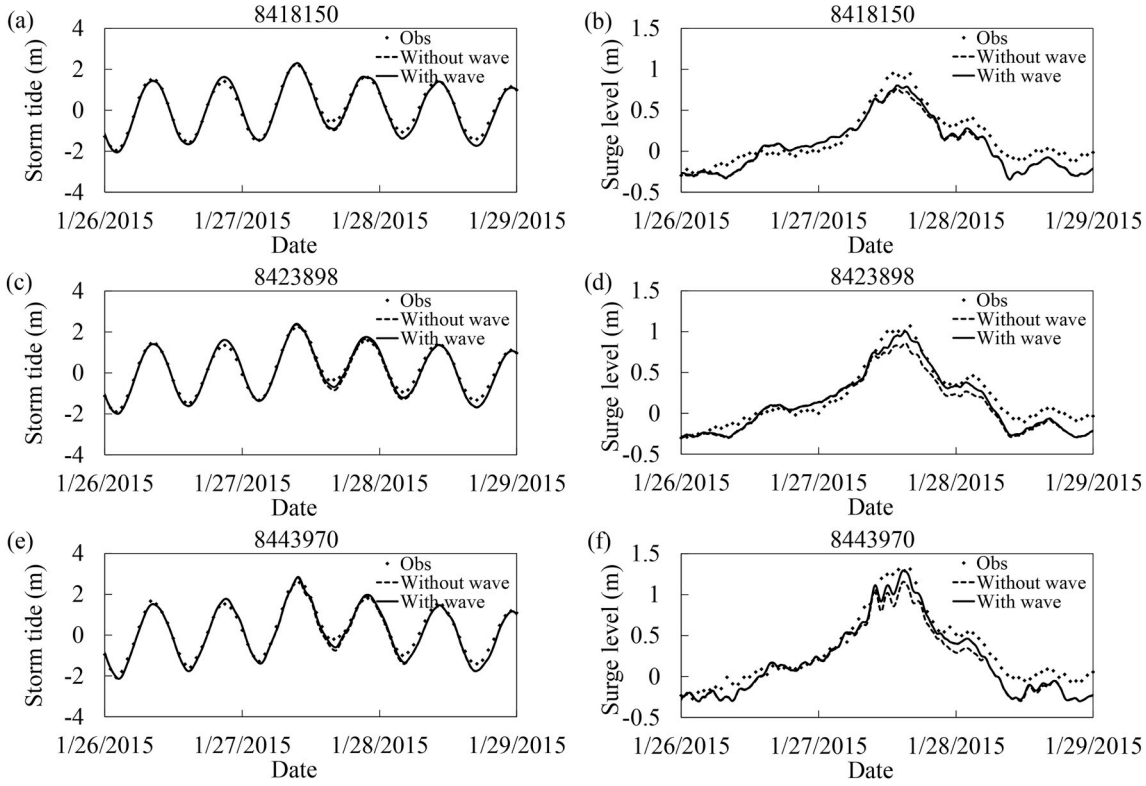

Fig. 8. Comparison of predicted (a)(c)(e) storm tide (total water level) and (b)(d)(f) storm surge with the observations by 3 tide gauges during the 2015 North American blizzard. The "Obs" for storm tide denotes the measured total water level by tide gauges (see Fig. 7b for locations and Table 3 for water depth). The "Obs" for surge level denotes the measurement by subtracting NOAA predicted tide from the total water level recorded by tide gauges. The black solid and dashed line labeled "With wave" and "Without wave" represents tide-surge simulation with and without wave effects.

and 8443970, accounting for 14 percent and 11 percent of the surge levels respectively. Along Scituate coast, the contribution of wave setup to the total water level depends on the local bathymetry and coastline geometry. The wave setup along the coast varied from 0.1 m to 0.25 m, which is significant compared to storm surge of approximately 1.0 m. The wave setup also varies with tidal phases as shown in Fig. B1 in Appendix B. At high tide, larger waves can reach the shore without breaking with increased water depth, which resulted in smaller wave setup. At low to mid-tide, the wave setup is more pronounced and reached up to 0.25 m at the seawall location. The increased wave setup was mainly contributed by: (1) the increased wave height offshore of Scituate because storm peak occurred at the rising mid-tide; (2) more pronounced depth-limited wave breaking due to smaller water depth at the coast than that at high tide. Lerma et al. (2018) found a difference of 5% in the forcing conditions (water level, wave height and period) can produce +13.5% differences in terms of water volume propagating in land. After January 28, the surge level was slightly underestimated. A possible cause is that the water level fluctuation generated by the wind and atmospheric pressure anomaly at the open ocean boundary played a significant role as the storm moved over the boundary, which was not incorporated along the boundary in the current model set.

Wave validation with 5 buoy measurements are shown in Fig. 9. Among the five buoys, buoy 44013 is located 16 km to the northeast of Scituate and is the closest to the study site (Fig. 7b). The wave height and period were well reproduced by model prediction with and without tide-surge effect, however, the simulation results were slightly improved when accounting for the tide-surge effect. The dual peaks observed and predicted at buoy 44008 are related to the location of the buoy relative to the passage of the storm. Buoy 44008 is only buoy located at the edge of the Gulf of Maine. The first wave peak at 44008 is generated by a long fetch from the east/northeast direction, similar with those buoys in the Gulf of Maine. However, when storm passed this buoy, a cyclonic wave feature was observed at this location, which resulted decrease and then increase in wave height. At other buoys in the Gulf of Maine except 44008, large waves were generated by a large wind fetch from the east/northeast direction during the passage of the storm. These buoys are located far from the storm track with consistent east/northeast wind fetch during the entire storm.

At buoy 44013, the inclusion of the tide-surge effect increased significant wave height by 0.85 m at the storm peak. The predicted peak wave period was also more accurate when the water level and current effects due to tide and surge were considered, which implies more accurate wave spectra predictions. Since the wave buoys are in relatively deep water (Table 2), the impact of tide-surge on waves is not as significant as that at the coast as shown in Fig. B1 and B2 in Appendix B, where the wave height is significantly modulated by tide-surge through water depth (Zou and Xie, 2016). The tidal modulation of waves along the Scituate is significant both at the coast and offshore as shown in Fig. B2. At high tide, the wave height was increased by 0.7–1.0 m at water depth greater than 10 m when the tide-surge effect was included. The tide-surge effect on waves was more pronounced at the coast, with increased wave height of 1.3–1.6 m, mainly due to less wave breaking with increased water depth. At low tide, the wave height was increased in the offshore region and decreased at the coast. Similarly, at falling and rising mid-water, the wave height increase was greater offshore than that at the coast. Appendix B presents more discussion on tide-surge and wave interaction and its impact on water level, circulation and wave height.

6. Wave overtopping in Scituate, Massachusetts

6.1. Wave overtopping prediction

The wave and water level computed by the coupled SWAN

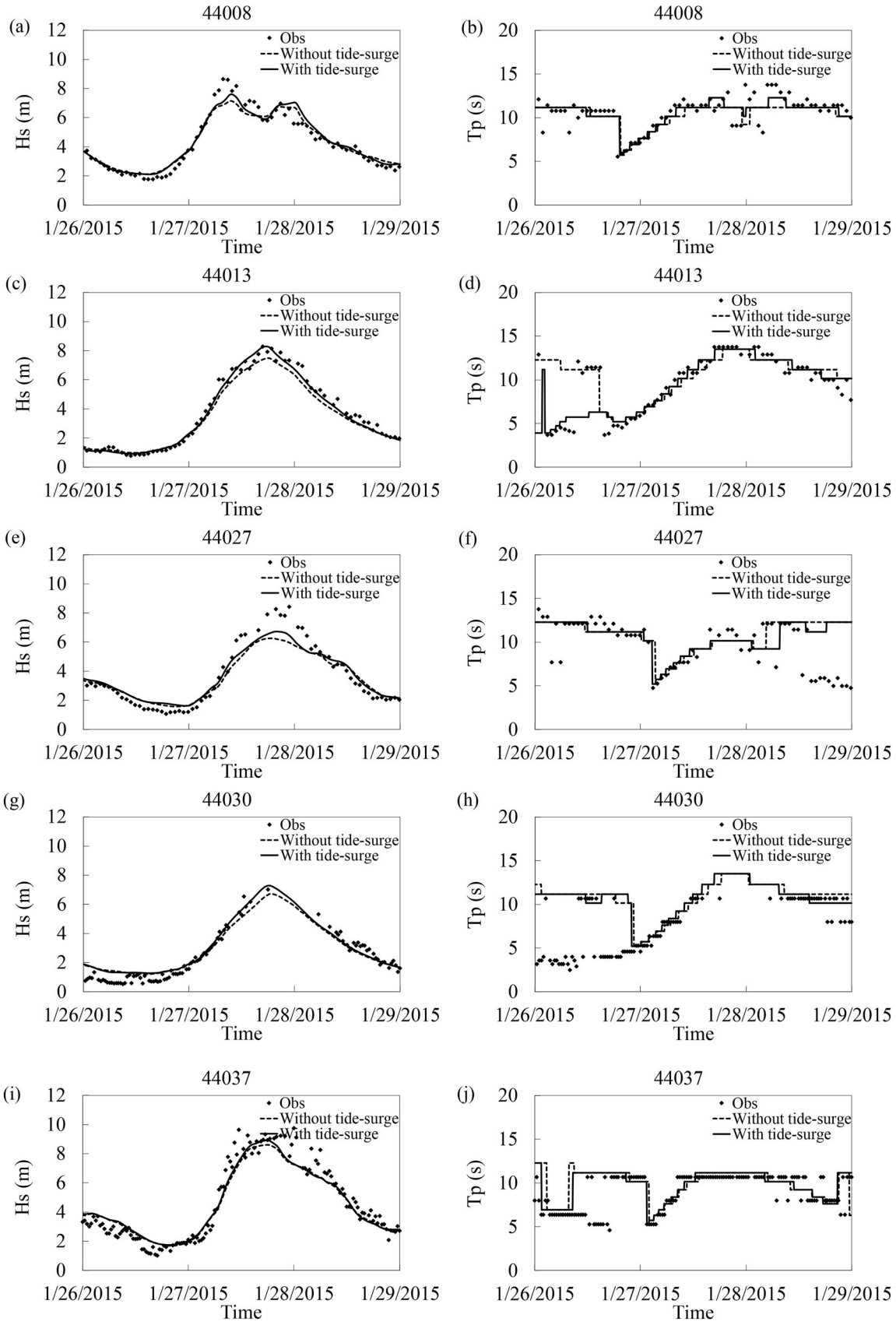

Fig. 9. Comparison of predicted significant wave height and peak wave period with the measurements of 5 wave buoys (see Fig. 7b for buoy locations and Table 2 for water depths) during the 2015 North American blizzard.

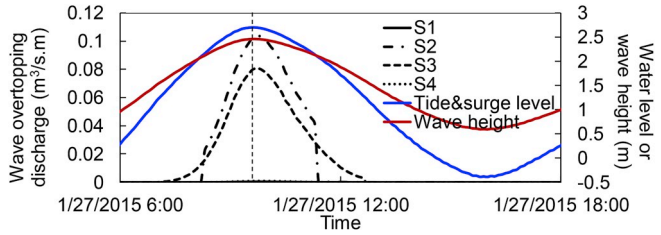

Fig. 10. Water level and wave overtopping discharge per unit length at the four survey locations S1−S4 along the Scituate seawall indicated in Fig. 2b. The tide &surge level and wave height were extracted at the toe of the steep slope in front of the seawall at S2 in the Avenues Basin from the surf zone model.

+ ADCIRC model were used to drive the surf zone model and wave overtopping model to simulate wave overtopping along the coast of Avenues Basin. The predicted water volume in the basin contributed by wave overtopping minus that by drainage was then compared with the volume calculated using the datalogger data.

Fig. 10 shows the wave overtopping discharges at the 4 survey locations during the tidal cycle when the storm surge and waves reached their peaks. At S2 and S3, the wave overtopping discharge reached 0.10 m^3/s.m and 0.08 m^3/s.m, while wave overtopping at S1 and S4 was negligible. The wave overtopping discharge was in phase with water level at the seawall toe. At the storm peak, the storm tide reached 2.71 m above local mean water level, resulting in a submerged seawall toe at S2 and S3, while the seawall toe at S1 and S4 was still emergent. Even though the waves had broken before they reached the structure, the elevated water level allowed larger waves to propagate further toward shore until they reached the seawall. Larger waves at the toe of the seawall produced significant overtopping at S2 and S3. The wave overtopping discharge at S2 increased more rapidly than that at S3 due to more vigorous wave breaking caused by the larger slope at S2.

Fig. 11 further demonstrates the relationships between seawall toe elevation, water level, waves and wave overtopping discharge at S2. Due to the phase difference between the peak swell waves offshore and the highest water level at the coast, the peak significant wave height at 10 m water depth lagged slightly behind the highest water level (Fig. 11a). However, the wave height was in phase with the total water

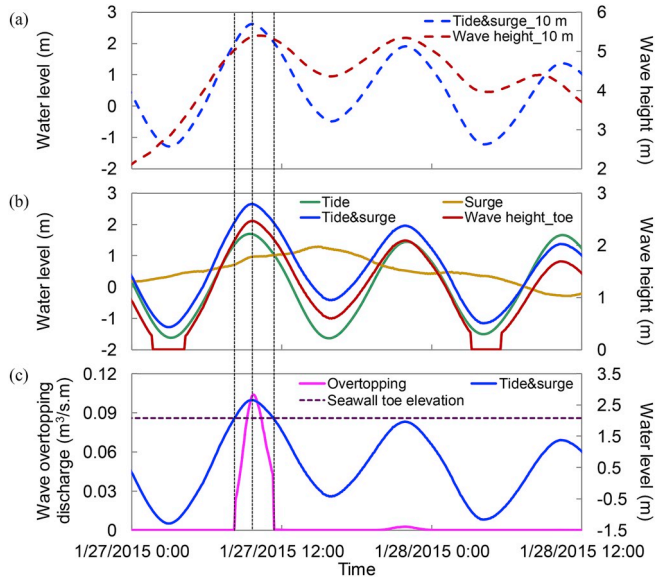

Fig. 11. Wave overtopping discharge per unit length, water level and significant wave height at 10 m water depth at near S2 location in front of the seawall in Scituate, Massachusetts (see Fig. 1b); . (a) Water level and significant wave height; (b) Water level (Tide&surge), tide, surge and significant wave height; (c) Wave overtopping discharge per unit length and Tide&surge level.

level at the toe of the steep slope in front of the seawall due to the modulation of water depth on wave height (Fig. 11b). While the peak surge level reached 1.30 m approximately 1 h before low tide, the highest water level coincided with high tide when the surge level was 0.97 m (Fig. 11b). Between 8:12 UTC and 11:24 UTC on 1/27/2015, the seawall toe at S2 became submerged. With increased water level during this period, the significant wave height at the toe of the integral structure increased accordingly. Large waves rushed up the structure, resulting in significant wave overtopping at this site.

6.2. Drainage parameterization

The water in the basin exits through (1) the drainage pipe; (2) the corridor at the southeast corner of the basin (Fig. 1b). Flooding occurs mainly because the drainage system was overwhelmed by overtopping water during the January 2015 North American blizzard. The drainage rate through the outlet pipe was 0.7 m^3/s during the January 2015 North American blizzard, which was smaller than its designed flow rate due to snow and debris in the pipe. The cross-section of the flow corridor at the southeast corner of the Avenues Basin was simplified as an isosceles trapezoid. The width of the bottom base of the corridor is 4.60 m at 4.36 m above the mean sea level and the base angle is 166° based on the USGS LIDAR data. Flood water flows through this corridor when the water level reaches 4.36 m above the mean sea level.

The drainage rate of the drainage pipe was determined by measurement in this study. The drainage rate of the corridor at the southeast corner of the basin was parameterized using Manning's equation (Henderson, 1966), in which the Manning roughness coefficient, the friction slope and the geometry of the corridor are required input parameters. The geometry of corridor is determined by the USGS LIDAR data. The Manning roughness coefficient is determined by the land cover (concrete). The predicted drainage rate of the corridor is not sensitive to these input parameters. For example, changing the base angle of the corridor from 135° to 166° only results in 10 percent difference in the flow rate. Also, a 10 percent change in the friction slope and Manning roughness coefficient results in less than 5 percent difference in the flow rate. The drainage rate was then calculated at the 6-min interval based on the measured water level in the basin using the drainage model described in Section 3.4. The drainage rate through the corridor increased rapidly after the water level reached 4.36 m above local mean sea level in the basin. When the water level reached its peak of 5.0 m above local mean sea level in the basin at 10:24 UTC on January 27, the discharge rate through the corridor was 19.0 m^3/s. The flow discharge rate through the outlet pipe was significantly lower than that via the corridor after the water level in the basin reached 4.36 m above the local mean sea level. The drainage system in the basin needs to be upgraded to cope with the flood risk by overtopping along the seawall in the basin.

6.3. Wave overtopping validation

The wave overtopping model computes overtopping discharge per meter length of the seawall. The total wave overtopping rate along the entire length of the seawall contributing to flooding the basin was calculated as follows:

$$Q_{total} = q_{S1}*72.8 + (q_{S2} + q_{S3})/2.0*343.7 + q_{S4}*32.8 \quad (11)$$

Where Q_{total} is the total wave overtopping rate along the seawall (m^3/s); q_{S1}, q_{S2}, q_{S3} and q_{S4} (m^3/s.m) are the wave overtopping rate per unit width at locations S1–S4 respectively; the constant coefficients, 72.8 m, 343.7 m and 32.8 m are the sectional length of the seawall marked in Fig. 1b. The peak value of wave overtopping rate along the seawall reached 35.0 m^3/s (Fig. 12a), which overwhelmed the drainage system in the basin.

Based on the wave overtopping and drainage prediction, the accumulated water volume in the basin was determined. Fig. 12 shows the

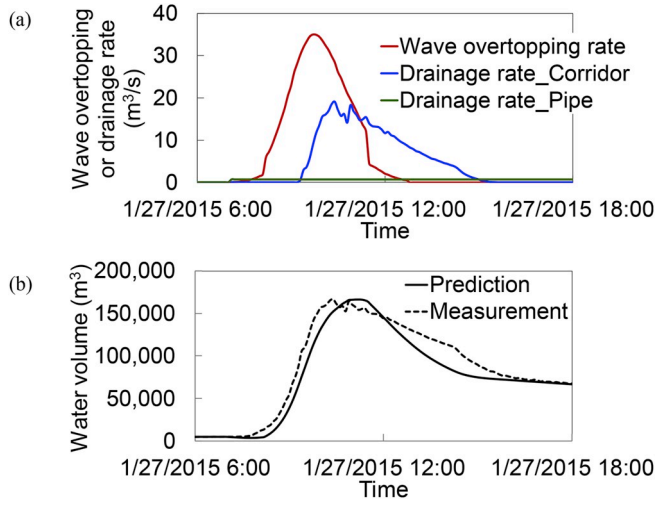

Fig. 12. Time evolution of total wave overtopping rate over the whole seawall in Scituate, Massachusetts (see Fig. 1b), and the comparison of predicted and measured volume of water in the Avenues Basin behind the seawall during the January 2015 North American blizzard. (a) Total wave overtopping rate, drainage through the corridor and drainage pipe. (b) Predicted and measured volume of water in the Avenues Basin. The solid line represents the model predictions, and the dashed line represents the field measurements.

comparison of water volume in the basin between the results based on measured water level and model prediction. The predicted water volume agrees well with that based on water level measurement. The measured water volume reached its peak of 166,509 m^3 at 10:24 UTC on 1/27/2015 and the predicted peak water volume was 166,124 m^3 at 11:12 UTC on 1/27/2015. While the magnitude of water volume agrees well, the predicted peak lags slightly behind the measurement data. Since waves are modulated by water level and wave overtopping mainly occurs during the rising and high water, a slight phase difference between the predicted water level and observed data may result in the shift of the predicted wave overtopping results. After the water volume reached its peak, the model predicted a rapid decrease of water volume in the basin. This may be partially attributed to the parameterization of flow rate through the corridor. Since the flow rate was calculated based on the water level recorded by the datalogger, there was a slight mismatch in phase with the overtopping prediction. Also, the flow was calculated as a uniform flow at every 6-min interval based on the water level at the beginning of the interval, which may result in under- or overestimation of flow rate during that interval. The nonlinear hydro-morphological interaction could potentially contribute to the slight mismatch, which was not considered in this study (Du et al., 2010). The water flows out of the corridor only when the water level in the basin reached 4.36 m above local mean sea level. The peak value of wave overtopping rate along the seawall reached 35.0 m^3/s (Fig. 12a), which overwhelmed the drainage system in the basin. The peak drainage rate in Fig. 12a corresponds to the peak water level/water volume in the basin in Fig. 12b which is determined by the difference between the overtopping and drainage and it lags the peak wave overtopping in Fig. 12a.

6.4. Impact of tide-surge and wave interaction on wave overtopping

Another numerical simulation was conducted to investigate the effect of tide-surge and wave interaction on wave overtopping. SWAN and ADCIRC were run independently for wave parameters and water level at the boundary of the surf zone model. The significant wave height, mean wave period and water level were then used as input for the surf zone model and wave overtopping model. The wave overtopping discharges were compared with the overtopping discharges obtained using the coupled SWAN + ADCIRC output as the input for the surf zone and overtopping models. The results from 8:18 UTC to 11:18 UTC on 1/27/2015 are shown in Fig. 13.

Fig. 13d indicates that the tide-surge and wave interaction increased the wave overtopping discharge by five folds. While the water level at the toe of the steep slope was similar in the two cases with relatively small wave effect (Fig. 13a), the wave height increased significantly with tide-surge and wave interaction (Fig. 13b). This is mainly due to the water level effect. The offshore boundary of surf zone model is located where the slope of bathymetry changes abruptly. The mean water depth ranges from 5.5 to 8.5 m, which is shallow enough for waves to be strongly modulated by tide and surge level (Zou et al., 2013). Even though the wave height was adjusted to deepwater wave height by including shoaling effects at these locations, the effect of water level cannot be eliminated.

The wave overtopping discharge is greatly affected by the significant wave height and relative freeboard at the toe of the structure (Van der Meer et al., 2016). On one hand, the decrease of 10 percent in the significant wave height will result in approximately 15 percent decrease in the wave overtopping discharge since the wave overtopping discharge is proportional to 2/3 power of the wave height. On the other hand, the wave overtopping discharge decreases exponentially with increased dimensionless relative freeboard due to the decrease of significant wave height (Fig. 13c). The decreased significant wave height also reduced the Iribarren number when the tide-surge and wave interaction was not included. The Iribarren number was larger than 2.0 when the interaction was included and smaller than 2.0 without the interaction when wave overtopping occurred. The combined effect of both smaller waves and more wave breaking contributed to a lower

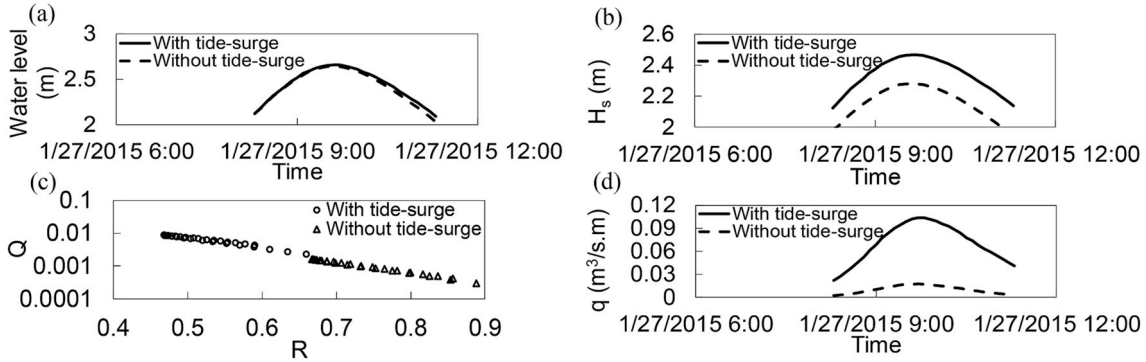

Fig. 13. Comparison of wave overtopping at S2 location in front of the seawall in Scituate, Massachusetts (see Fig. 1b) with and without the tide-surge and wave interaction. (a) Water level and (b) wave height at the toe of the steep slope of Seawall, (c) dimensionless overtopping discharge $Q= q/\sqrt{gH_{m0}^3}$ against the dimensionless relative freeboard $R= R_c/H_{m0}\xi_{m-1,0}$, (d) wave overtopping discharge. The black solid and dashed lines are results obtained using the coupled and non-coupled SWAN + ADCIRC results as the offshore boundary conditions for surf zone and wave overtopping models.

estimation of wave overtopping when the tide-surge and wave interaction was not included.

6.5. Impact of sea level rise and elevated seawall crest on wave overtopping

As mentioned in the introduction, Massachusetts is planning for a 0.25–2.08 m sea level rise along the coast by the year of 2100. By the year of 2050, the predicted sea level rise is 0.36 m for an intermediate sea level rise scenario. In this section, the impacts of 0.36 m rise in the sea level and the seawall crest height on wave overtopping were evaluated for a storm like the January 2015 North American blizzard.

The 0.36 m sea level rise was added to the mean sea level for the coupled SWAN + ADCIRC simulation to generate waves and water level for the surf zone and wave overtopping models. The increased sea level contributes to increased overtopping through: (1) increased significant wave height at the toe of the structure, and (2) decreased relative freeboard of the structure. Between 7:30 and 12:00 UTC on January 27, the water depth change at the toe of the structure with 0.36 m sea level rise fluctuated around 0.36 m due to the nonlinear interaction between water depth and tidal waves. The increased water depth at the toe of the seawall resulted in larger waves approaching the seawall. The significant wave height was increased between 0.2 m and 0.24 m (Fig. 14a). As explained in Section 6.3, the increase of 10 percent in the significant wave height will result in approximately 15 percent increase in wave overtopping discharge. The dimensionless relative freeboard is also significantly decreased with the 0.36 m sea level rise and the corresponding increase in the wave height. The lowest dimensionless relative freeboard decreases from 0.47 to 0.38 with the sea level rise (Fig. 14b). Due to the combination of these two contributing factors, the wave overtopping discharge doubled and reached 0.2 m^3/s.m with 0.36 m sea level rise at the storm peak (Fig. 14c).

Increasing the seawall crest elevation is an efficient way to reduce wave overtopping since it increases the relative freeboard. At the current sea level, raising the seawall crest by 0.36 m does not completely protect against flooding during a storm of this magnitude, although it would reduce discharge to about 75 percent of the current level at storm peak. The predicted wave overtopping discharge at the storm peak when both the sea level and the seawall crest elevation were increased by 0.36 m would increase roughly by 50 percent of the baseline case, or account for 75 percent of the overtopping discharge if the seawall crest is not raised. Fig. 14c indicates, however, the wave overtopping discharge would remain the same as the current level by raising the seawall crest by 0.9 m in a future scenario with a 0.36 m sea level rise (Fig. 14c).

7. Summary and conclusion

In the present study, the meteorological forcing was used to drive an integrated atmosphere-ocean-coast-overtopping modeling framework that consists the fully coupled SWAN + ADCIRC model, a surf zone and a wave overtopping model to predict the tide, surge and wave hydrodynamics and wave overtopping in the northeastern USA during the January 2015 North American blizzard.

At the coast, the interaction between tide-surge and waves has an important effect on the water level, waves, therefore overtopping. At a water depth less than 10 m, the wave height was increased by 1.3–1.6 m at high tide and decreased by 0.2 m at low tide. The wave setup along the coast varied from 0.1 m to 0.25 m depending on the coastline geometry and tidal phases. Larger wave setup was also observed at low and mid-tide than that at high tide, mainly due to the enhanced wave breaking at low and mid-tide.

The predicted wave and water level by the coupled SWAN + ADCIRC model were then used to drive the surf zone model to obtain the wave height at the toe of the steep beach slope in front of the seawall, which in turn was used to drive the wave overtopping model. Unlike previous studies such as Zou et al. (2013), the seawall was

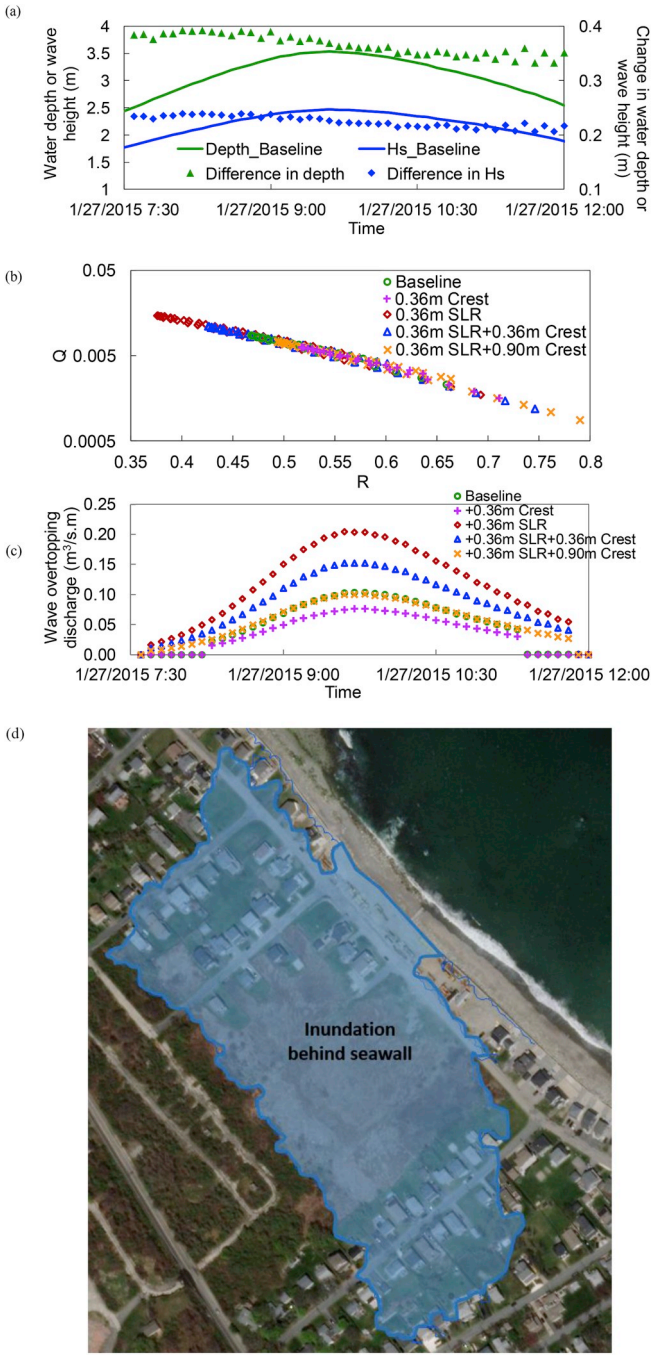

Fig. 14. Impact of sea level rise and seawall crest level on wave overtopping discharge at S2 location at Scituate seawall, MA, USA. (a) Water depth (green solid line) and significant wave height (Hs) (blue solid line) at the toe of the seawall without sea level rise, change in significant wave height (Hs) (blue diamonds) and water depth (green triangles) at the toe of the seawall in the presence of 0.36 m sea level rise (SLR), (b) dimensionless overtopping discharge against the dimensionless relative freeboard as defined in Fig. 13, (c) wave overtopping discharge with different combinations of sea level rise and crest elevation (Crest). (d) The estimated inundated area behind the seawall by a "bathtub" model at the storm peak of the January 2015 North American blizzard for the baseline (green circles in Fig. 14c, current seawall without sea level rise) and +0.36 m SLR + 0.90 m Crest (Orange × in Fig. 14c, 0.36 m sea level rise plus 0.90 m seawall crest elevation increase). (For interpretation of the references to colour in this figure legend, the reader is referred to the Web version of this article.)

treated as a wave wall, i.e. vertical wall on a steep slope embankment, to account for the steep beach slope in front of the Scituate seawall, MA.

Field measurements of water level collected by a Solinst LTC Levelogger Edge in the Avenues Basin behind the Scituate seawall in combination with a drainage model was used to estimate the measured wave overtopping discharge at the seawall. The model prediction agreed well with the field measurements for the January 2015 North American blizzard but with a slight shift in the timing of peak wave overtopping, which might have arisen from the slight phase shift of the predicted water level at the Scituate coast and the parameterization of drainage flow. The tide-surge and wave interaction increased the predicted wave overtopping discharge by five folds, mainly due to larger waves arriving at the seawall without breaking as a result of increased water depth by tide and surge.

The predicted wave overtopping at the Scituate seawall under different sea level rise and raised seawall crest scenarios indicated that a 0.36 m sea level rise in the future would double the peak overtopping discharge during a storm like the January 2015 North American blizzard. Wave overtopping discharge would increase by 50 percent if the seawall crest was raised by the same amount as the sea level rise, due to the increased wave height with the greater depth at the seawall toe. Since the wave overtopping discharge is the product of wave height to the power of 3/2 and the exponential function of wave height, it increases with wave height at a much faster rate than the water level. The model results indicate that increasing the seawall crest elevation by 0.9 m is required to keep the wave overtopping discharge at the current level in the scenario of 0.36 m sea level rise.

The present integrated multi-system modeling framework provides a useful planning tool to guide communities to upgrade their coastal defenses to adapt to the expected sea level rise. The model results show that the increased depth at the coastal structure due to sea level rise would not only decrease the free board but also increase the wave height. The latter causes the wave overtopping to increase at a much faster rate than the former so that coastal defenses will need to be raised much more than the expected rise in sea level.

In the presence of sea level rise, the overtopping discharge rate and therefore inundation is expected to increase significantly. However, once the elevation of the inundation behind the seawall exceeds the crest of the seawall, water in the Avenues Basin would overflow over the seawall and return to the ocean, which limits the maximum elevation of the inundation regardless the amount of sea level rise. The overflow discharge can be calculated based on the formula for overflow over a vertical weir (Lv et al., 2011). The overflow may also change the wave overtopping (Jones et al., 2013). The total water volume in the Basin should be estimated based on both the seaward overflow and shoreward wave overtopping as well as drainage.

The present study neglects the beach morphology changes during storms and storm clusters examined by Karunarathna et al. (2014) and Dissanayake et al. (2015) and with the sea level rise, which in turn change the hydrodynamics as shown by Peng et al. (2018). Also, the worst-case scenario when high surge coincides with the high tide, storm clusters, toe scour and beach lowering causing structural failure needs to be considered in the design of the seawall as an adaptation strategy to the future sea level rise.

Acknowledgments

This work was supported by the Maine Sea Grant and National Oceanic and Atmospheric Administration (Grants No. NA10OAR4170072). The first author was also supported by the Chase Distinguished Research Assistantship and the Michael J. Eckardt Dissertation Fellowship at the University of Maine. We would like to thank John Cannon at the National Weather Service, Bash Toulany and Will Perrie at Bedford Insitute of Oceanography, Chris Massey at the US Army Corps of Engineers, Bryan Pearce at University of Maine and Vijay Panchang at Texas A &M for helpful discussions. We also want to thank Neal Pettigrew at University of Maine for sharing wave buoy data for the validation of our wave predictions. The first author also wishes to thank Charlsye Diaz at the University of Maine for advice on technical writing. The scientific results and conclusions, as well as any view or opinions expressed herein, are those of the authors and do not necessarily reflect the views of NWS, NOAA, or the Department of Commerce. The authors wish to thank Mr. Stephen Cousins and Advanced Computing Group in The University of Maine System for the computational support.

Appendix A. The flowchart for wave overtopping prediction

The following flowchart illustrates the procedure to use the wave overtopping model for overtopping predictions for seawalls with the submerged or emerged toe. All the equations refer to the equations in Section 3.3 of the main context.

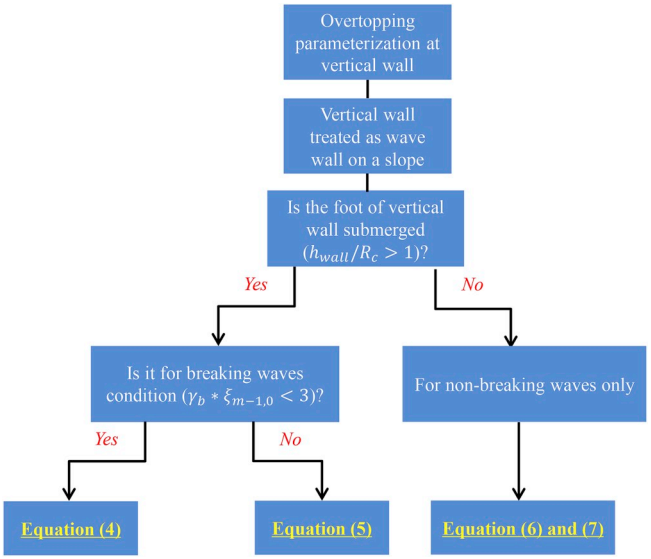

Where h_{wall} is the height of the wave wall, R_c is the crest freeboard, γ_b is the influence factor for a berm, $\xi_{m-1,0}$ is the breaker parameter.

Appendix B. Tide-surge and wave interaction at the Scituate coast

At the ocean surface, the presence of waves modifies the wind stress through ocean surface roughness (Janssen, 1991; Donelan et al., 1993; Taylor and Yelland, 2001; Drennan et al., 2003; Powell et al., 2003), therefore the storm surge (Brown and Wolf, 2009; Bertin et al., 2012). Waves also contribute to currents by wave radiation stress (Longuet-Higgins and Stewart, 1962, 1964; Mellor, 2005; Smith, 2006; Zou et al., 2006; Ardhuin et al., 2008) and Stokes Drift due to wave nonlinearity (Jenkins, 1987). The bottom friction experienced by mean current is also modified in the presence of waves (Grant and Madsen, 1979; Zou, 2004).

In shallow water, wave-current interaction is manifested through wave radiation stress and its horizontal gradients (Longuet-Higgins and Stewart, 1962, 1964), which significantly impact both water level and current through wave setup and set-down and by generating longshore current (Bowen, 1969; Longuet-Higgins, 1970). The water level affects wave propagation, refraction and breaking through water depth. The presence of current also results in wave refraction and wave frequency shifts (Komen et al., 1994).

B.1. Impact of waves on tide-surge

The impact of tide-surge and wave interaction on waves and circulation was analyzed at the Scituate coast. During the January 2015 North American blizzard, the peak wave height offshore of Scituate occurred at 18:00 UTC on January 27th when the total water level was close to mean sea level at the Scituate coast. The peak surge level appeared at 15:00 UTC on January 27th at low tide. The phase lag of peak wave and peak surge was mainly attributed to the modulation of water level on waves and storm surge. While peak surge level usually coincides with low tide, the peak wave appears when less depth-limited wave breaking happens. The wave and circulation fields were plotted at four tidal phases, i.e. high tide at 10:00 UTC 1/27/2015, falling mid-tide at 13:00 UTC 1/27/2015, low tide at 16:00 UTC 1/27/2015 and rising mid-tide at 19:00 UTC 1/27/2015, to analyze the interaction between tide-surge and waves over one tidal cycle.

The effect of waves on circulation at different tidal phases is shown in Fig. B1. The waves contribute to increased water level and current through wave radiation stress. The wave setup varied along the coast depending on the geometry of the coastline, as well as the wave-induced current. At high tide, the water depth was increased by 2.5 m at the coast, allowing large waves to propagate toward shore without breaking. The wave setup was thus expected to be smaller, with a magnitude of 0.15 m north of the headland in Scituate. A small clockwise circulation gyre also formed north of the headland due to waves, which tends to increase the water level at the south end of the gyre. At the three other tidal phases, the wave setup was more pronounced and reached 0.25 m north of the headland in general. The increased wave setup was mainly contributed by: (1) the increased wave height offshore of Scituate; (2) more pronounced depth-limited wave breaking due to smaller water depth at the coast compared to high tide. At low-tide and falling mid-tide, 0.05 m of wave set-down occurred at offshore of Scituate, and the wave-induced clockwise circulation gyre gradually disappeared. The onshore current due to waves intensified with increased wave height gradient in the cross-shore direction. Enhanced water level and circulation was identified due to wave effect in other open bays as well (Olabarrieta et al., 2014; Zou and Xie, 2016).

At the storm peak, the wave setup contributed approximately 0.3 m to the water level along the coast of the Avenues Basin. While the wind-driven current was to the south, the contribution of waves added complexity to the circulation field. A strong wave-induced current flowed in the onshore direction and gradually veered northward to the north of the headland in Scituate, and southward to the south of that point. The wind-driven current ranged from 0.2 m/s to 0.5 m/s. The wave-induced current reached 1.0 m/s and was dominant in the system.

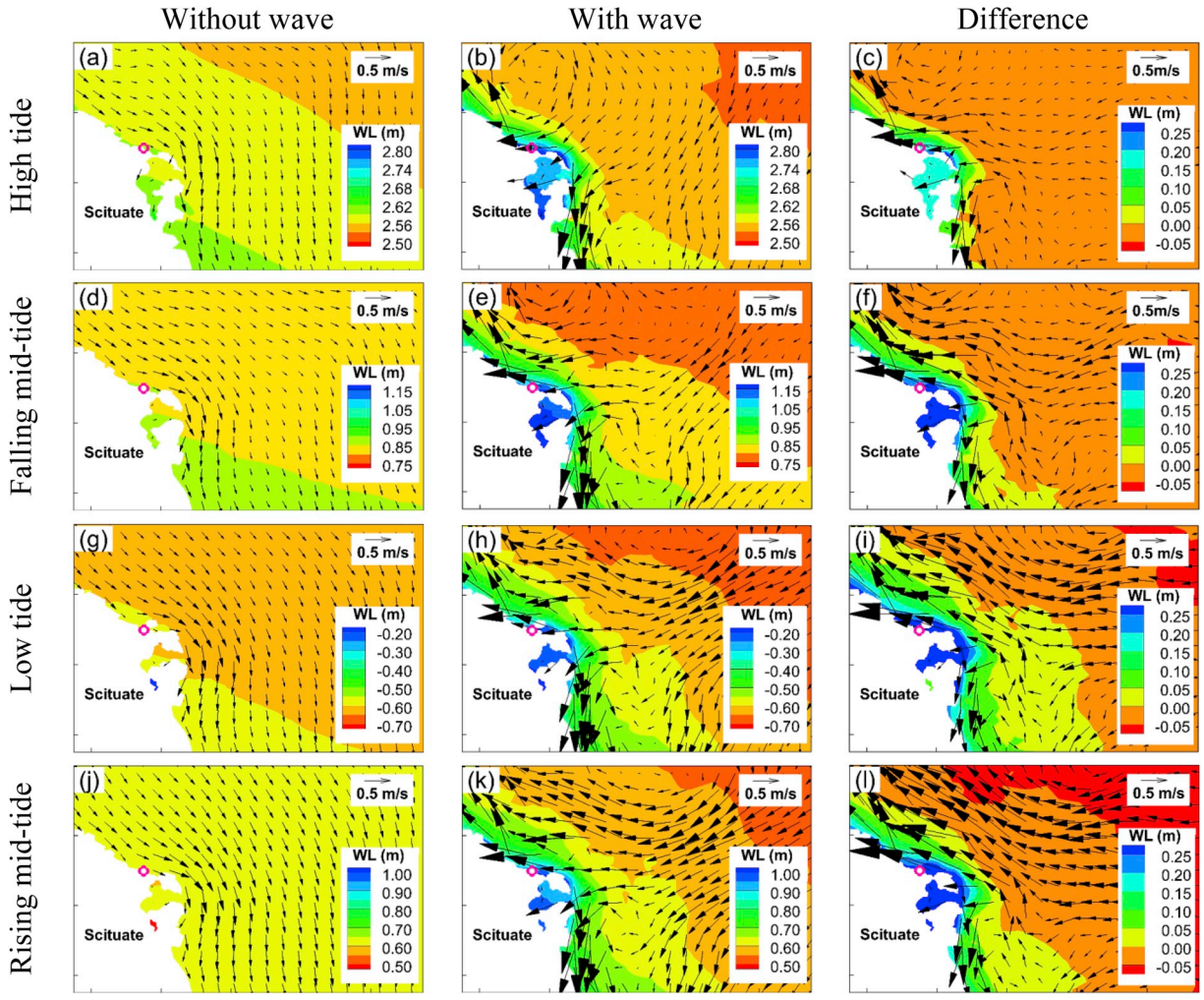

Fig. B1. Water level and circulation fields at four tidal phases during the January 2015 North American blizzard. (a)(b)(c) show water level and circulation fields at high tide at 10:00 UTC 1/27/2015, (d)(e)(f) show water level and circulation fields at falling mid-tide at 13:00 UTC 1/27/2015, (g)(h)(i) show water level and circulation fields at low tide at 16:00 UTC 1/27/2015, (j)(k)(l) show water level and circulation fields at rising mid-tide at 19:00 UTC 1/27/2015. The pink circle in the plots marks the location of the seawall.

B.2. Impact of tide-surge on waves

The modulation of tidal phases on waves is significant both at the coast and offshore (Fig. B2). At high tide, the wave height was increased by 0.7–1.0 m at water depth greater than 10 m when the tide-surge effect was included. The tide-surge effect on waves was more pronounced at the coast, with increased wave height of 1.3–1.6 m. This is mainly attributed to less wave breaking due to increased water depth. At low tide, the wave height was increased in the offshore region and decreased at the coast. Similarly, at falling and rising mid-water, the wave height increase was greater offshore than that at the coast.

When the significant wave height reached its peak offshore of Scituate at 18:00 UTC 1/27/2015, the impact of tide-surge and its associated current on waves was greater in deeper water than at the coast. In relatively deeper water, the significant wave height increased by 0.5 m–1.5 m with the tide-surge effect. At the coast, the impact of tide-surge was negligible because the wave height reached its peak near rising mid-tide. At this moment, the wave height at the coast was mainly limited by depth-induced wave breaking. The peak wave period increased by 2 s–4 s from offshore to the coast with tide-surge effect, while mean wave direction remained the same because it is mainly determined by wave refraction in shallow water and the wave crests were generally parallel to the depth contour lines.

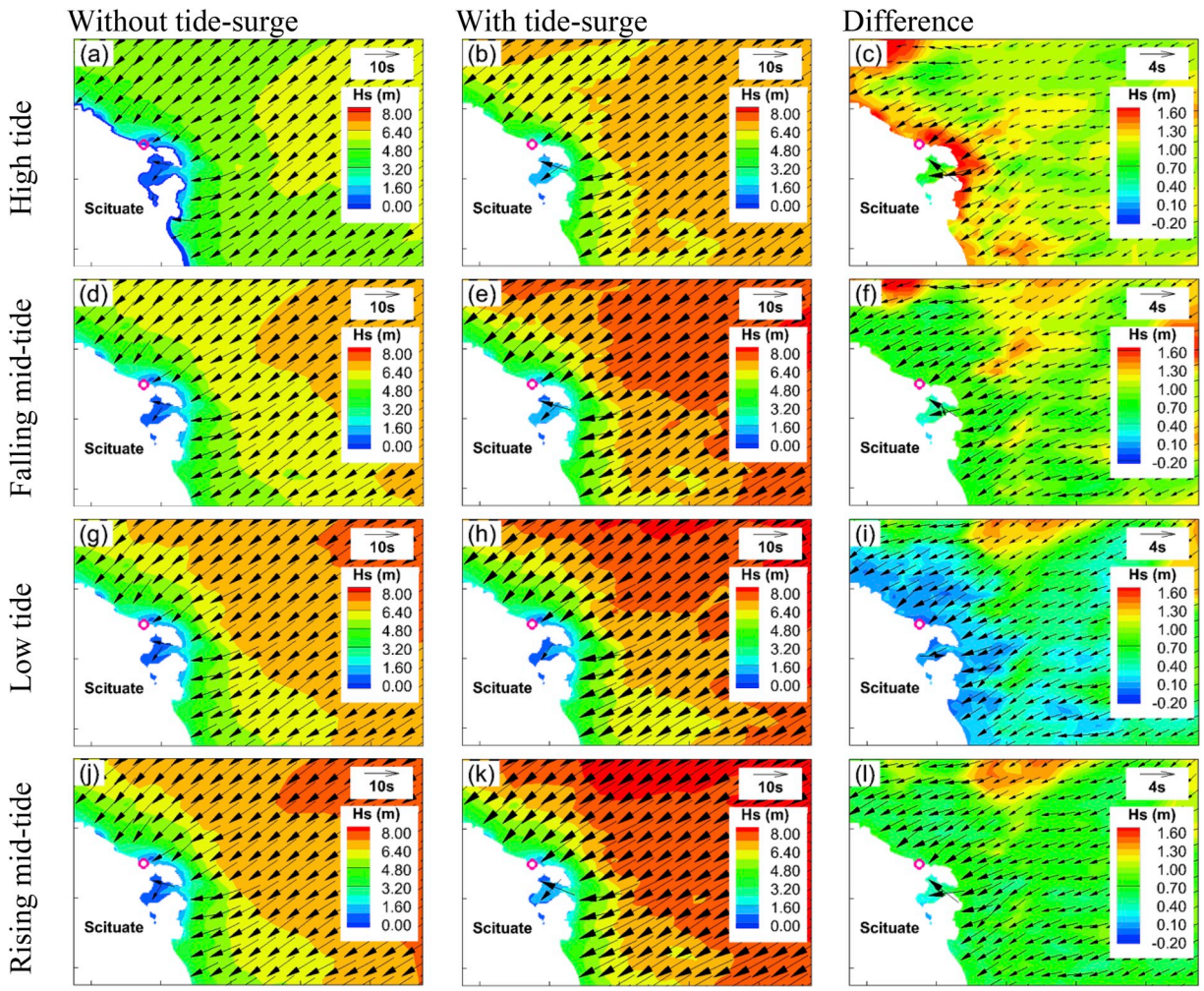

Fig. B2. Wave fields during the January 2015 North American blizzard. (a)(b)(c) show wave fields at high tide at 10:00 UTC 1/27/2015, (d)(e)(f) show wave fields at falling mid-tide at 13:00 UTC 1/27/2015, (g)(h)(i) show wave fields at low tide at 16:00 UTC 1/27/2015, (j)(k)(l) show wave fields at rising mid-tide at 19:00 UTC 1/27/2015. The pink circle in the plots marks the location of the seawall.

References

Amante, C., Eakins, B.W., 2009. ETOPO1 1 Arc-Minute Globe Relief Model: Procedures, Data Sources and Analysis. NOAA Tech. Memo. NESDIS NGDC-24, pp. 19.

Ardhuin, F., Rascle, N., Belibassakis, K.A., 2008. Explicit wave-averaged primitive equations using a generalized Lagrangian mean. Ocean Model. 20 (1), 35–60.

Bates, P.D., Dawson, R.J., Hall, J.W., Horritt, M.S., Nicholls, R.J., Wicks, J., Hassan, M.A.A.M., 2005. Simplified two-dimensional numerical modelling of coastal flooding and example applications. Coast. Eng. 52 (9), 793–810.

Battjes, J.A., Stive, M.J.F., 1985. Calibration and verification of a dissipation model for random breaking waves. J. Geophys. Res. Oceans 90 (C5), 9159–9167.

Bertin, X., Bruneau, N., Breilh, J.F., Fortunato, A.B., Karpytchev, M., 2012. Importance of wave age and resonance in storm surges: the case Xynthia, Bay of Biscay. Ocean Model. 42, 16–30.

Blain, C.A., Westerink, J.J., Luettich, R.A., 1994. The influence of domain size on the response characteristics of a hurricane storm surge model. J. Geophys. Res. Oceans 99 (C9), 18467–18479.

Booij, N., Ris, R.C., Holthuijsen, L.H., 1999. A third-generation wave model for coastal regions: 1. Model description and validation. J. Geophys. Res. Oceans 104 (C4), 7649–7666.

Bowen, A.J., 1969. Rip currents: 1. Theoretical investigations. J. Geophys. Res. 74 (23), 5467–5478.

Brocchini, M., Dodd, N., 2008. Nonlinear shallow water equation modeling for coastal engineering. J. Waterw. Port, Coast. Ocean Eng. 134 (2), 104.

Brown, J.M., Wolf, J., 2009. Coupled wave and surge modelling for the eastern Irish sea and implications for model wind-stress. Cont. Shelf Res. 29 (10), 1329–1342.

Bunya, S., Dietrich, J.C., Westerink, J.J., Ebersole, B.A., Smith, J.M., Atkinson, J.H., Jensen, R., Resio, D.T., Luettich, R.A., Dawson, C., Cardone, V.J., Cox, A.T., Powell, M.D., Westerink, H.J., Roberts, H.J., 2010. A high-resolution coupled riverine flow, tide, wind, wind wave, and storm surge model for southern Louisiana and Mississippi. Part I: model development and validation. Mon. Weather Rev. 138 (2), 345–377.

Cavaleri, L., Alves, J.H., Ardhuin, F., Babanin, A., Banner, M., Belibassakis, K., Benoit, M., Donelan, M., Groeneweg, J., Herbers, T.H.C., Hwang, P., Janssen, P.A.E.M., Janssen, T., Lavrenov, I.V., Magne, R., Monbaliu, J., Onorato, M., Polnikov, V., Resio, D., Rogers, W.E., Sheremet, A., McKee Smith, J., Tolman, H.L., van Vledder, G., Wolf, J., Young, I., 2007. Wave modelling-the state of the art. Prog. Oceanogr. 75 (4), 603–674.

Chen, H.F., Zou, Q.P., 2018. Characteristics of wave breaking and blocking by spatially varying opposing currents. J. Geophys. Res. Oceans 123 (5), 3761–3785.

Chen, Q., Kirby, J.T., Dalrymple, R.A., Kennedy, A.B., Chawla, A., 2000. Boussinesq modeling of wave transformation, breaking, and runup. II: 2D. J. Waterw. Port Coastal Ocean Eng. 126 (1), 48–56.

Chen, Q., Wang, L., Tawes, R., 2008. Hydrodynamic response of northeastern Gulf of Mexico to hurricanes. Estuar. Coasts 31 (6), 1098–1116.

Chen, C., Beardsley, R.C., Luettich, R.A., Westerink, J.J., Wang, H., Perrie, W., Xu, Q., Donahue, A.S., Qi, J., Lin, H., Zhao, L., Kerr, P.C., Meng, Y., Toulany, B., 2013. Extratropical storm inundation testbed: intermodel comparisons in Scituate, Massachusetts. J. Geophys. Res. Oceans 118 (10), 5054–5073.

Chen, J.L., Hsu, T.J., Shi, F., Raubenheimer, B., Elgar, S., 2015. Hydrodynamic and sediment transport modeling of New River Inlet (NC) under the interaction of tides and waves. J. Geophys. Res. Oceans 120 (6), 4028–4047.

Church, J.A., Clark, P.U., Cazenave, A., Gregory, J.M., Jevrejeva, S., Levermann, A., Merrifield, M.A., Milne, G.A., Nerem, R.S., Nunn, P.D., Payne, A.J., Pfeffer, W.T., Stammer, D., Unnikrishnan, A.S., 2013. Sea level change. In: Stocker, T.F., Qin, D., Plattner, G.-K., Tignor, M., Allen, S.K., Boschung, J., Nauels, A., Xia, Y., Bex, V., Midgley, P.M. (Eds.), Climate Change 2013: the Physical Science Basis, Contribution of Working Group I to the Fifth Assessment Report of the Intergovernmental Panel on Climate Change. Cambridge Univ. Press, Cambridge, UK, New York, NY, USA, pp. 1137–1216.

Dawson, C., Westerink, J.J., Feyen, J.C., Pothina, D., 2006. Continuous, discontinuous and coupled discontinuous-continuous Galerkin finite element methods for the

shallow water equations. Int. J. Numer. Methods Fluids 52 (1), 63–88.
Dean, R.G., Dalrymple, R.A., 1984. Water Wave Mechanics for Engineers and Scientists. Prentice-Hall, Englewood Cliffs, NJ, pp. 353.
Dietrich, J.C., Bunya, S., Westerink, J.J., Ebersole, B.A., Smith, J.M., Atkinson, J.H., Jensen, R., Resio, D.T., Luettich, R.A., Dawson, C., Cardone, V.J., Cox, A.T., Powell, M.D., Westerink, H.J., Roberts, H.J., 2010. A high-resolution coupled riverine flow, tide, wind, wind wave, and storm surge model for southern Louisiana and Mississippi. Part II: synoptic description and analysis of Hurricanes Katrina and Rita. Mon. Weather Rev. 138 (2), 378–404.
Dietrich, J.C., Zijlema, M., Westerink, J.J., Holthuijsen, L.H., Dawson, C., Luettich, R.A., Jensen, R.E., Smith, J.M., Stelling, G.S., Stone, G.W., 2011. Modeling hurricane waves and storm surge using integrally-coupled, scalable computations. Coast. Eng. 58 (1), 45–65.
Dietrich, J.C., Tanaka, S., Westerink, J.J., Dawson, C.N., Luettich, R.A., Zijlema, M., Holthuijsen, J.M., esterink, L.G., Westerink, H.J., 2012. Performance of the unstructured-mesh, SWAN+ ADCIRC model in computing hurricane waves and surge. J. Sci. Comput. 52 (2), 468–497.
Dissanayake, P., Brown, J., Karunarathna, H., 2015. Impacts of storm chronology on the morphological changes of the Formby beach and dune system, UK. Nat. Hazards Earth Syst. Sci. 15, 1533–1543.
Dodet, G., Bertin, X., Bruneau, N., Fortunato, A.B., Nahon, A., Roland, A., 2013. Wave-current interactions in a wave-dominated tidal inlet. J. Geophys. Res. Oceans 118 (3), 1587–1605.
Donelan, M.A., Dobson, F.W., Smith, S.D., Anderson, R.J., 1993. On the dependence of sea surface roughness on wave development. J. Phys. Oceanogr. 23 (9), 2143–2149.
Douglas, E., Jacobs, J., Hayhoe, K., Silka, L., Daniel, J., Collins, M., Alipour, A., Anderson, B., Hebson, C., Mecray, E., Mallick, R., 2017. Progress and challenges in incorporating climate change information into transportation research and design. J. Infrast. Syst 23 (4), 04017018.
Drennan, W.M., Graber, H.C., Hauser, D., Quentin, C., 2003. On the wave age dependence of wind stress over pure wind seas. J. Geophys. Res. Oceans 108, 8062.
Du, Y., Pan, S., Chen, Y., 2010. Modelling the effect of wave overtopping on nearshore hydrodynamics and morphodynamics around shore-parallel breakwaters. Coast. Eng. 57 (9), 812–826.
Egbert, G.D., Bennett, A.F., Foreman, M.G., 1994. TOPEX/POSEIDON tides estimated using a global inverse model. J. Geophys. Res. Oceans 24, 821–852.
Emanuel, K.A., 2013. Downscaling CMIP5 climate models shows increased tropical cyclone activity over the 21st century. Proc. Natl. Acad. Sci. U.S.A. 110 (30), 12219–12224.
Gallien, T.W., 2016. Validated coastal flood modeling at Imperial Beach, California: comparing total water level, empirical and numerical overtopping methodologies. Coast. Eng. 111, 95–104.
Gallien, T.W., Sanders, B.F., Flick, R.E., 2014. Urban coastal flood prediction: integrating wave overtopping, flood defenses and drainage. Coast. Eng. 91, 18–28.
Garratt, J.R., 1977. Review of drag coefficients over oceans and continents. Mon. Weather Rev. 105 (7), 915–929.
Goda, Y., 1975. Irregular wave deformation in the surf zone. Coast. Eng. Jpn. 18, 13–26.
Goda, Y., 2009. A performance test of nearshore wave height prediction with CLASH datasets. Coast. Eng. 56 (3), 220–229.
Grant, W.D., Madsen, O.S., 1979. Combined wave and current interaction with a rough bottom. J. Geophys. Res. Oceans 84 (C4), 1797–1808.
Hagen, S., Westerink, J., Kolar, R., Horstmann, O., 2001. Two-dimensional, unstructured mesh generation for tidal models. Int. J. Numer. Methods Fluids 35 (6), 669–686.
Hasselmann, K., Barnett, T.P., Bouws, E., Carlson, H., Cartwright, D.E., Enke, K., Ewing, J.A., Gienapp, H., Hasselmann, D.E., Kruseman, P., Meerburg, A., Müller, P., Olbers, D.J., Richter, K., Sell, W., Walden, H., 1973. Measurements of wind-wave growth and swell decay during the joint north sea wave project (JONSWAP). Dtsch. Hydrogr. Z. Suppl. 8A (12), 95.
Hedges, T.S., Reis, M.T., 1998. Random wave overtopping of simple seawalls a new regression model. Water Marit. Energy J. 157, 113–122.
Heidemann, H.K., 2014. Lidar Base Specification Version 1.2 (November 2014), Chapter 4 of Section B, U.S. Geological Survey Standards, Book 11, Collection and Delineation of Spatial Data. U.S. Geological Survey Techniques and Methods, pp. 67. Available online at: http://pubs.usgs.gov/tm/11b4/.
Henderson, F.M., 1966. Open Channel Flow. Macmillan Publ. Co., New York, N.Y., pp. 522.
Higuera, P., Lara, J.L., Losada, I.J., 2013. Simulating coastal engineering processes with OpenFOAM®. Coast. Eng. 71, 119–134.
Hu, K., Mingham, C.G., Causon, D.M., 2000. Numerical simulation of wave overtopping of coastal structures using the non-linear shallow water equations. Coast. Eng. 41 (4), 433–465.
Janssen, P.A.E.M., 1991. Quasi-linear theory of wind-wave generation applied to wave forecasting. J. Phys. Oceanogr. 21 (11), 1631–1642.
Jenkins, A.D., 1987. A Lagrangian model for wind- and wave-induced near-surface currents. Coast. Eng. 11 (5), 513–526.
Ji, C., Zhang, Q., Wu, Y., 2017. Derivation of three-dimensional radiation stress based on Lagrangian solutions of progressive waves. J. Phys. Oceanogr 47 (11), 2829–2842.
Jones, D.K., Zou, Q., Reeve, D.E., 2013. Computational modelling of coastal flooding caused by combined surge overflow and wave overtopping on embankments. J. Flood Risk Manag. 6 (2), 70–84. https://doi.org/10.1111/j.1753-318X.2012.01155.x.
Karunarathna, H., Pender, D., Ranasinghe, R., Short, A.D., Reeve, D.E., 2014. The effects of storm clustering on beach profile variability. Mar. Geol. 348, 103–112.
Kennedy, A.B., Chen, Q., Kirby, J.T., Dalrymple, R.A., 2000. Boussinesq modeling of wave transformation, breaking, and runup. I: 1D. J. Waterw. Port Coastal Ocean Eng. 126 (1), 39–47.
Kennedy, A.B., Westerink, J.J., Smith, J.M., Hope, M.E., Hartman, M., Taflanidis, A.A., Tanaka, S., Westerink, H., Cheung, K.F., Smith, T., Hamann, M., Minamide, M., Ota, A., Dawson, C., 2012. Tropical cyclone inundation potential on the Hawaiian islands of oahu and kauai. Ocean Model. 52, 54–68.
Kirshen, P., Watson, C., Douglas, E., Gontz, A., Lee, J., Tian, Y., 2008. Coastal flooding in the Northeastern United States due to climate change. Mitig. Adapt. Strategies Glob. Change 13 (5–6), 437–451.
Komen, G.J., Cavaleri, L., Donelan, M., Hasselmann, K., Hasselmann, S., Janssen, P.A.E.M., 1994. Dynamics and Modelling of Ocean Waves. Cambridge Univ. Press, Cambridge, pp. 532.
Lara, J.L., Garcia, N., Losada, I.J., 2006. RANS modelling applied to random wave interaction with submerged permeable structures. Coast. Eng. 53 (5), 395–417.
Lerma, A.N., Bulteau, T., Elineau, S., Paris, F., Durand, P., Anselme, B., Pedreros, R., 2018. High-resolution marine flood modelling coupling overflow and overtopping processes: framing the hazard based on historical and statistical approaches. Nat. Hazards Earth Syst. Sci. 18 (1), 207.
Lim, E., Taylor, L.A., Eakins, B.W., Carignan, K.S., Warnken, R.R., Medley, P.R., 2009. Digital Elevation Model of Portland, Maine: Procedures, Data Sources and Analysis. National Oceanic and Atmospheric Administration Technical Memorandum NESDIS NGDC-30, U.S, pp. 29.
Lin, P., Liu, P.L.F., 1998. A numerical study of breaking waves in the surf zone. J. Fluid Mech. 359 (1), 239–264.
Lin, N., Kopp, R., Horton, B., Donnelly, J., 2016. How does hurricane sandy's flood frequency change from 1800 to 2100? Proc. Natl. Acad. Sci. U.S.A. 113 (43), 12071–12075.
Longuet-Higgins, M.S., 1970. Longshore currents generated by obliquely incident sea waves: 1. J. Geophys. Res. 75 (33), 6778–6789.
Longuet-Higgins, M.S., Stewart, R.W., 1962. Radiation stress and mass transport in gravity waves, with application to 'surf beats'. J. Fluid Mech. 13 (04), 481–504.
Longuet-Higgins, M.S., Stewart, R.W., 1964. Radiation stresses in water waves; a physical discussion, with applications. Deep Sea Res. 11 (4), 529–562.
Losada, I.J., Lara, J.L., Guanche, R., Gonzalez-Ondina, J.M., 2008. Numerical analysis of wave overtopping of rubble mound breakwaters. Coast. Eng. 55 (1), 47–62.
Luettich, R.A., Westerink, J.J., 2004. Formulation and Numerical Implementation of the 2D/3D ADCIRC Finite Element Model Version 44.XX. pp. 74. Available online at: http://adcirc.org/adcirc_theory_2004_12_08.pdf.
Lv, X., Zou, Q.P., Reeve, D., 2009. A hybrid LS and VOF method for 3-D simulation of wave breaking and overtopping. Int. J. Offshore Polar 19 (4), 308–316.
Lv, X., Zou, Q., Reeve, D.E., 2011. Numerical simulation of overflow at vertical weirs using a hybrid level set/VOF method. Adv. Water Resour. 34 (10), 1320–1334. https://doi.org/10.1016/j.advwatres.2011.06.009.
Lynett, P.J., Melby, J.A., Kim, D.-H., 2010. An application of Boussinesq modeling to Hurricane wave overtopping and inundation. Ocean Eng. 37 (1), 135–153.
Massachusetts Office of Coastal Zone Management (MACZM), 2013a. Mapping and Analysis of Privately-Owned Coastal Structures along the Massachusetts Shoreline. pp. 76. Available online at: http://www.mass.gov/eea/docs/czm/stormsmart/seawalls/private-coastal-structures-2013.pdf.
Massachusetts Office of Coastal Zone Management (MACZM), 2013b. Sea Level Rise: Understanding and Applying Trends and Future Scenarios for Analysis and Planning. pp. 22. Available online at: http://www.mass.gov/eea/docs/czm/stormsmart/slr-guidance-2013.pdf.
Massachusetts Office of Coastal Zone Management (MACZM), 2016. Coastal Erosion, Sediment Transport, and Prioritation Management Strategy Assessment for Shoreline Protection. Scituate, Massachusetts, pp. 199. Available online at: https://www.scituatema.gov/sites/scituatema/files/file/file/scituateprioritization_finalreport_august2016_compress_main.pdf.
Massachusetts Department of Conservation and Recreation (MADCR), 2009. Massachusetts coastal infrastructure inventory and assessment project. pp. 76. Available online at: http://www.mass.gov/eea/docs/czm/stormsmart/seawalls/public-inventory-report-2009.pdf.
Marsooli, R., Lin, N., 2018. Numerical modeling of historical storm tides and waves and their interactions along the U.S. East and Gulf Coasts. J. Geophys. Res. Oceans 123 (5), 3844–3874.
McCabe, M.V., Stansby, P.K., Apsley, D.D., 2013. Random wave runup and overtopping a steep sea wall: shallow-water and Boussinesq modelling with generalised breaking and wall impact algorithms validated against laboratory and field measurements. Coast. Eng. 74, 33–49.
Mellor, G., 2005. Some consequences of the three-dimensional current and surface wave equations. J. Phys. Oceanogr. 35 (11), 2291–2298.
National Research Council, 2009. Mapping the Zone: Improving Flood Map Accuracy. The National Academies Press, Washington, DC.
Nicholls, R.J., 2002. Analysis of global impacts of sea-level rise: a case study of flooding. Phys. Chem. Earth 27 (32), 1455–1466.
NOAA National Centers for Environmental Information (NCEI), 2018. U.S. Billion-dollar weather and climate disasters (2018). Retrieved from NOAA website: https://www.ncdc.noaa.gov/billions/.
Olabarrieta, M., Geyer, W.R., Kumar, N., 2014. The role of morphology and wave-current interaction at tidal inlets: an idealized modeling analysis. J. Geophys. Res. Oceans 119, 8818–8837.
Orton, P.M., Hall, T.M., Talke, S., Blumberg, A.F., Georgas, N., Vinogradov, S., 2016. A validated tropical-extratropical flood hazard assessment for New York harbor. J. Geophys. Res. Oceans 121 (12), 8904–8929.
Papoulis, A., Pillai, S.U., 2002. Probability, Random Variables, and Stochastic Processes. Tata McGraw-Hill Education.
Pawlowicz, R., Beardsley, B., Lentz, S., 2002. Classical tidal harmonic analysis including error estimates in MATLAB using T_TIDE. Comput. Geosci. 28 (8), 929–937.
Peng, Z., Zou, Q.P., 2011. Spatial distribution of wave overtopping water behind coastal

structures. Coast. Eng. 58, 489–498.
Peng, Z., Zou, Q.P., Lin, P.Z., 2018. A partial cell technique for modeling the morphological change and scour. Coast. Eng. 131, 88–105.
Powell, M.D., Vickery, P.J., Reinhold, T.A., 2003. Reduced drag coefficient for high wind speeds in tropical cyclones. Nature 422 (6929), 279–283.
Pugh, D.T., 1987. Tides, Surges and Mean Sea level: a Handbook for Engineers and Scientists. John Wiley & Sons, New York, N.Y., pp. 472.
Reeve, D.E., Soliman, A., Lin, P.Z., 2008. Numerical study of combined overflow and wave overtopping over a smooth impermeable seawall. Coast. Eng. 55 (2), 155–166.
Raby, A., Jayaratne, R., Bredmose, H., Bullock, G., 2019. Individual violent wave-overtopping events: behaviour and estimation. J. Hydraul. Res. https://doi.org/10.1080/00221686.2018.1555549.
Ris, R.C., Holthuijsen, L.H., Booij, N., 1999. A third-generation wave model for coastal regions: 2. Verification. J. Geophys. Res. Oceans 104 (C4), 7649–7666.
Roberts, K.J., Colle, B.A., Korfe, N., 2017. Impact of simulated twenty-first-century changes in extratropical cyclones on coastal flooding at the Battery, New York City. J. Appl. Meteorol. Climatol. 56 (2), 415–432.
Saha, S., Moorthi, S., Wu, X., Wang, J., Nadiga, S., Tripp, P., Behringer, D., Hou, Y., Chuang, H., Iredell, M., Ek, M., Meng, J., Yang, R., Mendez, M.P., van den Dool, H., Zhang, Q., Wang, W., Chen, M., Becker, E., 2014. The NCEP climate forecast system version 2. J. Clim. 27 (6), 2185–2208.
Sallenger Jr., A.H., 2000. Storm impact scale for barrier islands. J. Coast Res. 890–895.
Shao, S.D., Ji, C., Graham, D.I., Reeve, D.E., James, P.W., Chadwick, A.J., 2006. Simulation of wave overtopping by an incompressible SPH model. Coast. Eng 53 (9), 723–735.
Shi, F., Kirby, J.T., Harris, J.C., Geiman, J.D., Grilli, S.T., 2012. A high-order adaptive time-stepping TVD solver for Boussinesq modeling of breaking waves and coastal inundation. Ocean Model. 43, 36–51.
Smit, P., Zijlema, M., Stelling, G., 2013. Depth-induced wave breaking in a non-hydrostatic, near-shore wave model. Coast. Eng. 76, 1–16.
Smith, J.A., 2006. Wave-current interactions in finite depth. J. Phys. Oceanogr. 36, 1403–1419.
Sun, Y., Perrie, W., Toulany, B., 2018. Simulation of wave-current interactions under hurricane conditions using an unstructured-grid model: impacts on ocean waves. J. Geophys. Res. Oceans 123, 3739–3760.
Taylor, P.K., Yelland, M.J., 2001. The dependence of sea surface roughness on the height and steepness of the waves. J. Phys. Oceanogr. 31 (2), 572–590.
Thornton, E.B., Guza, R.T., 1983. Transformation of wave height distribution. J. Geophys. Res. Oceans 88 (C10), 5925–5938.
Tsoukala, V.K., Chondros, M., Kapelonis, Z.G., Martzikos, N., Lykou, A., Belibassakis, K., Makropoulos, C., 2016. An integrated wave modelling framework for extreme and rare events for climate change in coastal areas–the case of Rethymno, Crete. Oceanologia 58 (2), 71–89.
Twomey, E.R., Signell, R.P., 2013. Construction of a 3-arcsecond Digital Elevation Model for the Gulf of Maine. Open-File Report 2011-1127 US Geological Survey, pp. 24. Available online at: https://pubs.usgs.gov/of/2011/1127/.
Van der Meer, J.W., Allsop, N.W.H., Bruce, T., De Rouck, J., Kortenhaus, A., Pullen, T., Schüttrumpf, H., Troch, P., Zanuttigh, B., EurOtop, 2016. Manual on Wave Overtopping of Sea Defences and Related Structures. An Overtopping Manual Largely Based on European Research, but for Worldwide Application. Available online at: www.overtopping-manual.com.
Wang, P., Sheng, J., 2016. A comparative study of wave-current interactions over the eastern Canadian shelf under severe weather conditions. J. Geophys. Res. Oceans 121, 5252–5281.
Wang, Z., Zou, Q.P., Reeve, D.E., 2009. Simulation of spilling breaking waves using a two-phase flow CFD model. Comput. Fluids 38 (10), 1995–2005.
Wang, P., Sheng, J., Hannah, C., 2017. Assessing the performance of formulations for nonlinear feedback of surface gravity waves on ocean currents over coastal waters. Cont. Shelf Res. 146, 102–117.
Warner, J.C., Sherwood, C.R., Signell, R.P., Harris, C.K., Arango, H.G., 2008. Development of a three-dimensional, regional, coupled wave, current, and sediment-transport model. Comput. Geosci. 34 (10), 1284–1306.
Wei, G., Kirby, J.T., Grilli, S.T., Subramanya, R., 1995. A fully nonlinear Boussinesq model for surface waves. Part 1. Highly nonlinear unsteady waves. J. Fluid Mech. 294 (13), 71–92.
Westerink, J.J., Luettich, R.A., Muccino, J.C., 1994. Modelling tides in the western north atlantic using unstructured graded grids. Tellus 46 (2), 178–199.
Westerink, J.J., Luettich, R.A., Feyen, J.C., Atkinson, J.H., Dawson, C., Roberts, H.J., Powell, M.D., Dunion, J.P., Kubatko, E.J., Pourtaheri, H., 2008. A basin- to channel-scale unstructured grid hurricane storm surge model applied to southern Louisiana. Mon. Weather Rev. 136 (3), 833–864.
Wolf, J., 2009. Coastal flooding: impacts of coupled wave–surge–tide models. Nat. Hazards 49 (2), 241–260.
Woodruff, J.D., Irish, J.L., Camargo, S.J., 2013. Coastal flooding by tropical cyclones and sea-level rise. Nature 504 (7478), 44–52.
Xie, D.M., Zou, Q.P., Cannon, J.W., 2016. Application of SWAN+ ADCIRC to tide-surge and wave simulation in Gulf of Maine during Patriot's Day storm. Water Sci. Eng. 9 (1), 33–41.
Yang, Z., Myers, E.P., 2008. Barotropic tidal energetics and tidal datums in the Gulf of Maine and Georges Bank region. In Estuarine and Coastal Modeling 2007. ASCE, pp. 74–94.
Zhang, Y., Baptista, A.M., 2008. SELFE: a semi-implicit Eulerian-Lagrangian finite-element model for cross-scale ocean circulation. Ocean Model. 21 (3–4), 71–96.
Zhang, F., Li, M., Ross, A.C., Lee, S.B., Zhang, D., 2017. Sensitivity analysis of hurricane arthur (2014) storm surge forecasts to WRF physics parameterizations and model configurations. Weather Forecast. 32 (5), 1745–1764.
Zijlema, M., 2010. Computation of wind-wave spectra in coastal waters with SWAN on unstructured grids. Coast. Eng. 57 (3), 267–277.
Zijlema, M., Stelling, G.S., 2008. Efficient computation of surf zone waves using the nonlinear shallow water equations with non-hydrostatic pressure. Coast. Eng. 55 (10), 780–790.
Zou, Q.P., 2004. A simple model for random wave bottom friction and dissipation. J. Phys. Oceanogr. 34 (6), 1459–1467.
Zou, Q.P., Peng, Z., 2011. Evolution of wave shape over a low-crested structure. Coast. Eng. 58, 478–488.
Zou, Q.P., Xie, D.M., 2016. Tide-surge and wave interaction in the Gulf of Maine during an extratropical storm. Ocean Dynam. 66 (12), 1715–1732.
Zou, Q.P., Bowen, A.J., Hay, A.E., 2006. The vertical distribution of wave shear stress in variable water depth: theory and field observations. J. Geophys. Res. Oceans 111, C09032.
Zou, Q.P., Chen, H., 2017. Wind and current effects on extreme wave formation and breaking. J. Phys. Oceanogr. 47 (7), 1817–1841.
Zou, Q.P., Chen, Y., Cluckie, I., Hewston, R., Pan, S., Peng, Z., Reeve, D., 2013. Ensemble prediction of coastal flood risk arising from overtopping by linking meteorological, ocean, coastal and surf zone models. Q. J. Roy. Meteorol. Soc. 139 (671), 298–313.